Metal Structures as Advanced Materials in Nanotechnology

19

Angelo Accardo, Remo Proietti Zaccaria, Patrizio Candeloro, Francesco Gentile, Maria Laura Coluccio, Gobind Das, Roman Krahne, Carlo Liberale, Andrea Toma, Simone Panaro, Ermanno Miele, Manohar Chirumamilla, Vijayakumar Rajamanickam, and Enzo Di Fabrizio

Keywords

Plasmonics • Chemical mapping • SERS • Superhydrophobic • DNA templating • Fractal • Electroless • Superclusters • Nanoantenna • Electron beam lithography • Plasmon-polariton modes

Introduction: The Importance of Metal Nanostructures as Advanced Materials

Metal nanostructures can play an important role in a variety of topics ranging from near-field imaging and tip spectroscopy (TERS or SPPERS) [1–10], surface-enhanced Raman spectroscopy (SERS) [11–13], to energy efficiency of devices such as solar panels or batteries [14], photocatalysis [15, 16], and electric transport [17]. The morphology of the metallic nanostructures must be tailored according to the chosen application, for example, metal nanoparticles can be well suited for SERS analysis while metallic thin films can be more suitable for solar harvesting.

A. Accardo (✉) • R. Proietti Zaccaria • G. Das • R. Krahne • C. Liberale • A. Toma • S. Panaro • E. Miele • M. Chirumamilla • V. Rajamanickam
Nanostructures Department, Italian Institute of Technology, Genoa, Italy
e-mail: angelo.accardo@iit.it; remo.proietti@iit.it; gobind.das@iit.it; roman.krahne@iit.it; carlo.liberale@iit.it; andrea.toma@iit.it; simone.panaro@iit.it; ermanno.miele@iit.it; manohar.chirumamilla@iit.it; vijayakumar.rajamanickam@iit.it

P. Candeloro • F. Gentile • M.L. Coluccio
BioNEM Laboratories, Department of Experimental and Clinical Medicine, University Magna Graecia of Catanzaro, Catanzaro, Italy
e-mail: patrizio.candeloro@unicz.it; gentile@unicz.it; mlcoluccio@gmail.com

E. Di Fabrizio
Physical Science & Engineering Division, King Abdullah University of Science and Technology, Thuwal, Kingdom of Saudi Arabia
e-mail: enzo.difabrizio@kaust.edu.sa

B. Bhushan et al. (eds.), *Handbook of Nanomaterials Properties*,
DOI 10.1007/978-3-642-31107-9_42,

Morphology can also be tuned for enhancing the photo–chemi–electric properties of the nanostructures. For example, the catalytic performance strongly depends on the exposed area of the metallic nanostructure, while its photonic properties greatly depend on the resonance conditions which, in turn, are related to the geometrical characteristics of the nanostructure. Other examples of metallic structure, where the optical and electric properties are related to each other, are metallic photonic crystals which have applications in areas such as filters, optical switches, cavities, and efficient laser designs [18]. Such metallic crystals are particularly attractive because of their ability to control electronic and photonic resonances simultaneously. Therefore, such structures may open up further impressive possibilities for tailoring the light–matter interaction [19].

When it comes to choose an appropriate metal for realizing photo–chemi–electric nanodevices, two materials are among the most common choices: silver and gold. Silver nanostructures are best known for their morphology-dependent optical properties like surface plasmon resonances (SPRs). They also serve as very efficient substrates for SERS and are the most efficient catalyst for epoxidation of ethylene. Furthermore, silver is very often chosen for photo-applications in the visible range, ought to its low absorption. Similarly, gold nanostructures are very attractive due to their excellent chemical stability, bio-inertness, SPRs/SERS properties, and unique catalytic activity. These aspects are also the reason of using gold for photo-applications in the visible range, even though it shows a higher absorption peak than silver.

A number of techniques can be followed in order to realize metallic nanostructures; however, the fabrication of nanodevices can be categorized in two main groups: top-down and bottom-up. The former makes use of lithographic techniques in order to mold a 'brick' of material to the final desired product [20, 21], while the latter reaches the same goal by moving atoms or molecules into place by means of special tools such as atomic force microscope and scanning tunneling microscope [22], through self-organization techniques [23–29], or by means of alternative methods as the shadow mask deposition [30] or even by using DNA [31].

To date, the bottom-up nanoscale manufacturing is not as controllable as the top-down one which makes the latter approach the main choice for a number of applications, especially when reproducibility is an important issue. For this reason we shall mainly focus on this manufacturing method where techniques such as electron beam lithography and focus ion beam have been employed guaranteeing a reproducibility of devices down to the nanometers. In particular, in section 'Micro- and Nanofabrication Methods for Devices at the Nanoscale: Silver Nanoclusters, Metal Nanoparticles, and 3D Plasmonic Design' we will give a brief overview of representative microfabrication processes related to metal nanoparticles and nanostructures design followed, in section 'Characterization, Physical, and Chemical Properties of Metal Nanostructures as a Function of the Size, Shape, and Formation Conditions', by the description of a number of physical mechanisms related to nanoparticles aggregation at the nanoscale and nanowires templating. Finally, in section 'Properties, Specific Physical Effects of Metal Nanostructures, and the Case of Surface Plasmon Resonance', we will focus on the specific case of metal nanostructured plasmonic devices.

Micro- and Nanofabrication Methods for Devices at the Nanoscale: Silver Nanoclusters, Metal Nanoparticles, and 3D Plasmonic Design

Electroless Metal Deposition

A chemical/electroless deposition process is a novel deposition technique whereby metal ions are reduced as atoms and deposited on a solid surface, specifically a metal, a semiconductor, or also a plastic material. The electroless process is considered very attractive because it is of simple realization, it does not need expensive or specialized equipment, and it enables the contemporary fabrication of a great quantity of nanoparticles and then of patterned substrates. This makes it interesting for the large-scale production in electronic, catalysis, or optical devices fabrication. Furthermore, in nanotechnology, the great uniqueness of this method is that it allows precise control over the nucleation and growth of nanoparticles. In this technique, a metal salt precursor is reduced in solution in the presence of a stabilizing agent, which prevents aggregation and improves the chemical stability of the formed nanoparticles. Explicitly, metal ions are reduced to metals by a reducing agent that is simply an electron donor while the metal ions are electron acceptors. The reaction rate is often accelerated by a catalyst on which both the surface metal ions and the reducing agent are adsorbed to facilitate the transfer of electrons. Minute amounts of the deposited metal catalyze the reaction, and thus, the deposition itself becomes autocatalytic. Electroless deposition can therefore continue indefinitely, provided that the metal ions and the reducing agents are replenished [32]. Using electroless techniques, several metals may be deposited, including silver, gold, copper, nickel, or their alloys, thus obtaining thin films, sub-micrometric metallic structures, or nanoparticles [33–36].

In the particular case of electroless deposition, the reducing agent is the surface where the metal has to be deposited. A typical example is the silver deposition on a silicon substrate. The scheme of the silver electroless chemical reaction is briefly recapitulated in Figs. 19.1 and 19.2.

When a silicon substrate is dipped in a solution of fluoridric acid (HF) and silver nitrate ($AgNO_3$) (a typical composition is [HF] = 0.15 M and [$AgNO_3$] = 1 mM), silicon reduces silver ions to the metallic form, as described by the following chemical reaction [37–40]:

$$4Ag^{+} + Si(s) + 6HF \rightarrow 4Ag^{0} + H_2SiF_6 + 4H^{+} \tag{19.1}$$

which can be separated into two half-cell reactions, that is, the Si oxidation at the anode

$$Si + 2H_2O \rightarrow SiO_2 + 4H^{+} + 4e^{-} \tag{19.2}$$

and the Ag reduction, at the cathode

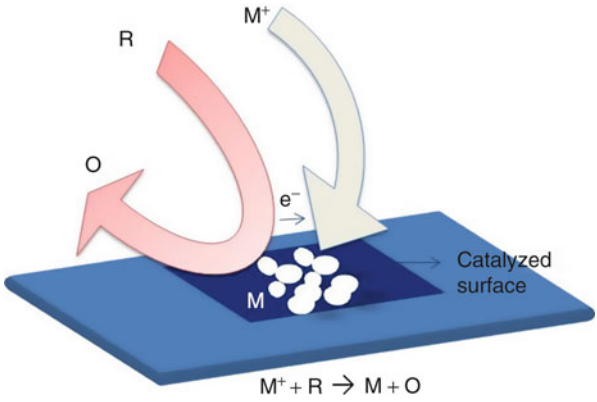

Fig. 19.1 Schematic representation of an electroless process where metal ions (M^+) are reduced by the electrons given from oxidation of a reducing species (R)

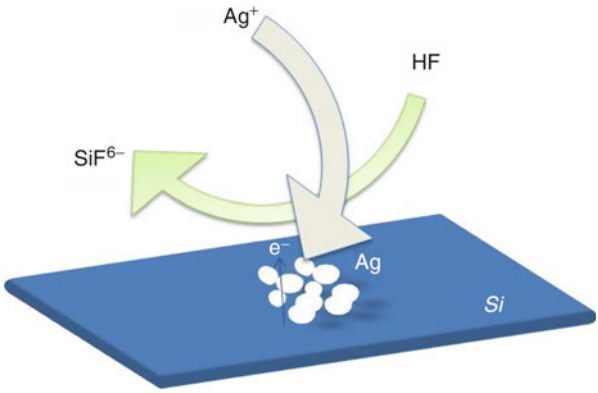

Fig. 19.2 Schematic representation of silver electroless deposition on a silicon substrate into a HF solution

$$Ag^+ + e^- \rightarrow Ag^0 \tag{19.3}$$

The role of HF in solution is to remove both the superficial silicon oxide (SiO_2) and the SiO_2 which is formed from silicon oxidation consequently to the electroless process. Upon the immersion in the fluoridric acid solution, the following reaction takes place:

$$SiO_2 + 6HF \rightarrow 2H^+ + SiF_6{}^{2-} + 2H_2O. \tag{19.4}$$

Here, the formation of Si–F superficial bonds is expected because thermodynamically favourable, nevertheless the acid environment of the solution causes a consistent polarization of $Si^{\delta+}$–$F^{\delta-}$ determining the weakening of the bulk Si–Si bonds. In these conditions, HF could easily react with the substrate, according to a nucleophilic attack, producing a hydrogenated silicon surface, as described by

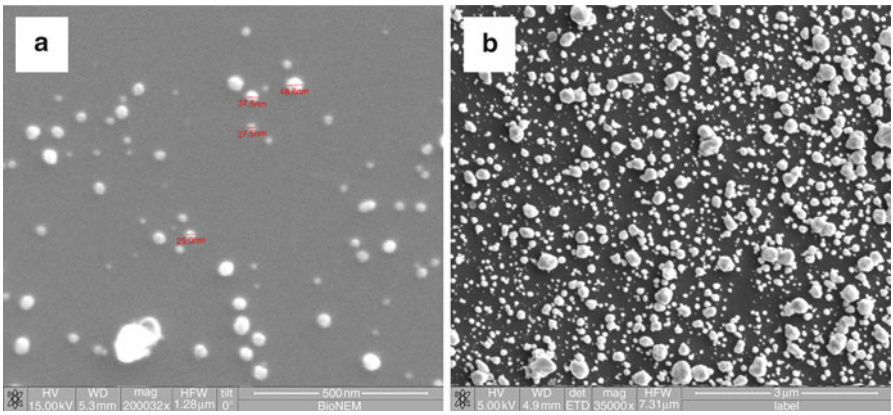

Fig. 19.3 SEM micrographs of silver deposition: (**a**) on a silicon surface, operative conditions HF 0.15 M $AgNO_3$ 1 mM 50 °C 1 min and (**b**) on a silicon surface, operative conditions HF 0.15 M $AgNO_3$ 1 mM 50 °C 5 min

$$Si_{bulk} - Si - Si^{\delta+-}F^{\delta-} + HF \rightarrow Si_{bulk} - Si - H + F - Si - F. \tag{19.5}$$

This hydrogenated silicon surface is inert to reactions with O_2, CO_2, CO, etc., while presenting a good reactivity with silver ions [38]. The presence of HF gives force to the deposition process and it is important for plating large surfaces.

The mechanism of metal deposition sees, on a first stage, the nanoparticles formation by the direct reaction of some silver ions with the silicon substrate, forming metallic nuclei. These Ag nuclei are strongly electronegative, and because of this, they attract other electrons from silicon bulk becoming negatively charged; then, new silver ions react with disposable electron on the silver grains, reducing to Ag^0 and thus inducing the growth of the original Ag nuclei [41]. An autocatalytic mechanism is therefore generated, which continues also when all the silicon surface has been covered by silver, until electrons can be attracted from the silicon bulk.

The morphology of electroless nanoparticles and their aggregates depends on a variety of factors, including the pH of solution, the temperature T of the system, the total time t of the process, and the metal concentration c in solution (Fig. 19.3).

The rate of the reactions is regulated by a balance between thermodynamics and kinetics, and these parameters are closely correlated [42]. In particular, the driving force of the charge exchange is the difference between the redox potentials of the redox species in solution. The redox potential at equilibrium could be calculated approximately by using the Nernst relationship:

$$E = E^0 + \frac{RT}{nF} \ln \frac{[\text{Ox}]}{[\text{Red}]} \tag{19.6}$$

in which E is equilibrium potential, R is the ideal gas constant 8.314 J K^{-1} mol^{-1}, F is the Faraday constant 96,500 C mol^{-1}, T is the absolute temperature, and

[Ox] and [Red] are the molarities of the oxidized and reduced species in solution, respectively.

Equation 19.6 for the metal ions becomes

$$E = E^0 + \frac{RT}{F} \ln[M^+].$$

Considering the total redox reaction of the process, the Nernst equation expresses the relation between the equilibrium constant (K_e) and the redox potential (ΔE):

$$\ln K_e = \frac{nF\Delta E}{RT} \tag{19.7}$$

This equation evidences parameters like the concentrations of the ions in solution and the temperature of the system. It influences also the reaction's yield and the shape and size of the metal nanoparticles aggregates.

These considerations make electroless deposition a technique interesting for the realization of nanoparticles aggregates of specific shape and size, by means of the regulation of the process parameters. Using different growth conditions, metal nanoparticle aggregates may therefore grow within well-defined patterns. Recent advances in nanofabrication techniques, especially electron beam lithography (EBL), focused ion beam (FIB), and two-photon lithography (2PL), have improved the fabrication of patterned substrates [43–45]. These techniques afford exact control over the shape and size of bidimensional (in the case of EBL), and sometimes three-dimensional (in the case of FIB and 2PL), patterns at the nanoscale [42, 46]. Electroless deposition represents indeed a good method for assembling metal nanocluster into lithographic patterns, with extreme precision (Fig. 19.4).

Examples of typical parameters of deposition for metals such as silver and gold are reported in Table 19.1.

Novel 3D Nanoscale Plasmonic Device Design

There have been many efforts through traditional lithography technique for 3D microfabrication techniques such as self-assembly, μ stereo, ink-jet printing, layer by layer, holography and phase mask, LIGA (lithography, electroplating, and molding), optical sintering, and electron/ion beam lithographies, which proved their significant potential with the following limitations: (i) periodicity, (ii) limited 3D complexity, and (iii) lack of mechanical constraints. Apparently, by adapting and/or integrating one or more lithographic modalities working on a different scale would overcome these limits and advance the 3D nano-biotech research by lifting up as 3D emerging techniques.

Here, we present novel integrated nanoplasmonic structures obtained by lithographic methods on an optical tweezers (OT)-based 3D micromanipulator [47].

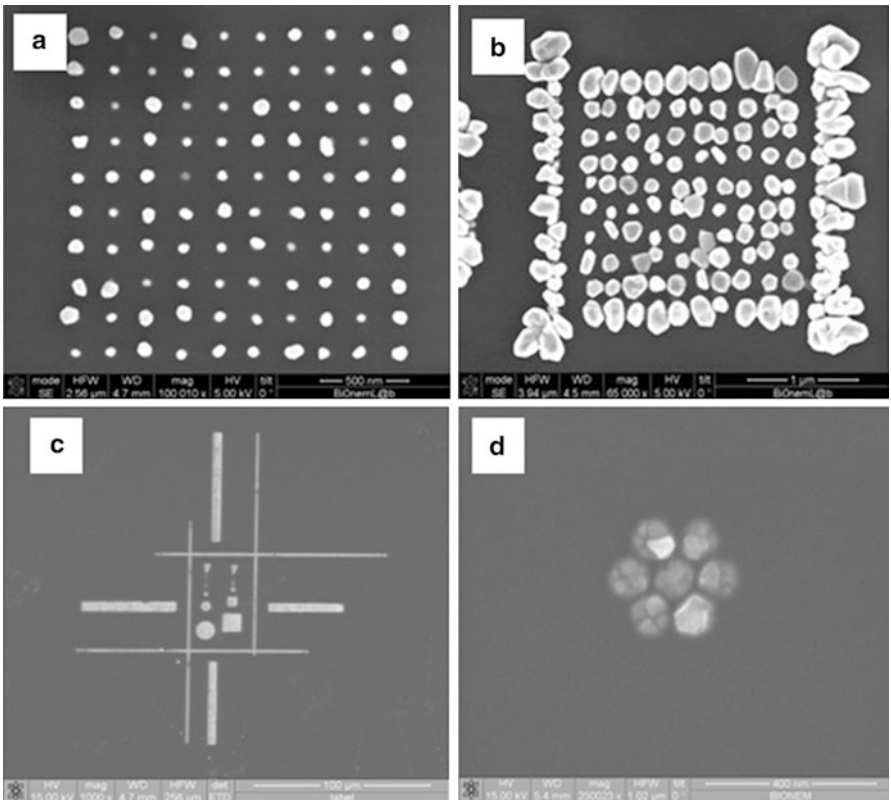

Fig. 19.4 SEM micrographs of metal deposition: (**a**) silver on a patterned silicon surface (*circular holes* with diameter 40 nm), operative conditions HF 0.15 M $AgNO_3$ 1 mM 50 °C 5 s; (**b**) silver on a patterned silicon surface (*circular holes* with diameter 40 nm), operative conditions HF 0.15 M $AgNO_3$ 0.05 mM 50 °C 50 s; (**c**) gold on a patterned silicon surface (*circular and quadrate holes*), operative conditions HF 0.15 M $HAuCl_4$ 1 mM 50 °C 3 min; and (**d**) silver on a patterned silicon surface (*structures with holes* of 100 nm diameter), operative conditions (i) first step HF 0.15 M 50 °C 1 min and (ii) second step $AgNO_3$ 0.003 mM 50 °C 40 s

Table 19.1 Typical parameters for silver and gold electroless deposition on silicon substrate

Deposition solutions
Silver: HF 0 ÷ 0,15 M, [$AgNO_3$] 0.1 ÷ 1 mM
Gold: HF 0 ÷ 0,15 M, [$HAuCl_4$] 0.1 ÷ 1 mM
Operative conditions
T = 0 ÷ 50 °C, time = 10 ÷ 60 s

The combination of different lithographic methods, also working on different scales, appears to be a very powerful strategy to increase the degrees of freedom for the fabrication of 3D micro- and nanostructures. These kinds of structures are of great interest, as they enable to add plasmonic functions to a probe that can be manipulated by using optical tweezers (OT) [48–52].

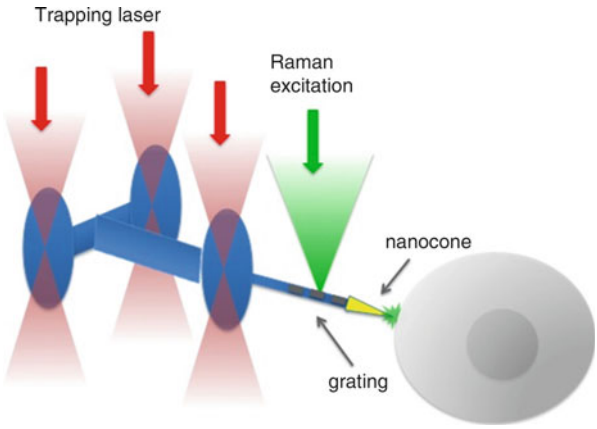

Fig. 19.5 Asymmetrical bead design

At first glance, the common spherical beads (most often polystyrene or silica beads) used with OT seem to be not the best structure or geometry on which to add a plasmonic probing part. An important drawback of the spherical beads is, in fact, related to the lack of an effective mechanism to fully control in the 3D space their orientation. This aspect is very important during the physical approach of the bead, carrying the plasmonic probe, to the sample to be measured. A second important issue comes from the observation that, when an optically trapped bead is close to a cell in suspension, the latter will be also attracted by the optical trap due to the closeness of the trapping point and the plasmon excitation point, preventing an accurate positioning of the plasmonic probing part with respect to the sample.

Because of these reasons, we choose to create an asymmetric bead with a larger main body, where it is optically trapped, and a long thin arm, on top of which there will be the plasmonic nanocone, which extends away from the position of the trapping laser focus. More precisely, we choose a design with three different trapping points and a protruding arm (a schematic of the asymmetrical beads and the optical traps is shown in Fig. 19.5).

These asymmetrical structures are fabricated by using the two-photon lithography (TPL) [53] method. This technique is intrinsically a 3D structuring process, since the photo-polymerizable resist is exposed only in the focus spot of an intense laser beam and relies on a straightforward process that allows creating structures that would be very complex or even impossible to fabricate with conventional lithographic methods [54, 55]. Moreover, as recently demonstrated, the spatial resolution attainable using TPL is sub-100 nm using laser wavelengths around 800 nm, which is well below the diffraction limit [56]. The custom made setup used for fabrication is schematized in Fig. 19.6.

A 100 fs pulse width, 80 MHz Ti–Sapphire laser oscillator (Tsunami, Spectra-Physics) is used as the excitation source for two-photon photopolymerization, and its central wavelength is tuned to around 720 nm. The output laser power at the back

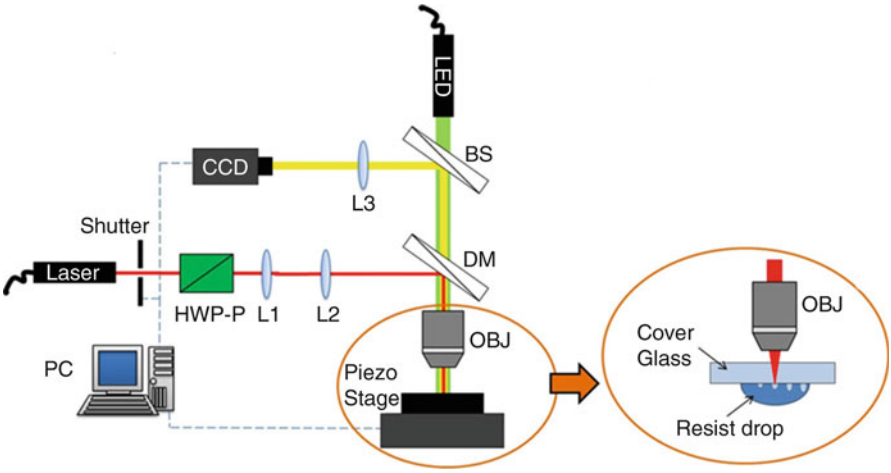

Fig. 19.6 Schematic of the two-photon lithography setup

focal plane of the microscope objective is controlled by using a variable attenuator made by an achromatic half-waveplate and a polarizer. The exposure time for each pixel is controlled through a computer-driven mechanical shutter. The beam is expanded and collimated by a telescope in order to obtain overfilling of the focusing microscope objective. Further, laser beam is reflected by a 45° dichroic mirror directly onto the objective back aperture. The dichroic mirror reflects most of the NIR laser beam and transmits part of the visible spectrum (400–550 nm) to a CCD camera which is used to check the position of the beam focus and for real-time monitoring of the photopolymerization process. The laser is focused by using a dry semi-apochromatic microscope objective (Olympus, LUCPlanFLN 60×, NA = 0.70) equipped with a spherical aberration correction collar.

A suitable coverslip holder is mounted on a xyz piezo stage (Tritor 101, Piezosystem Jena) for positioning in horizontal and vertical directions. The travel range of the piezo stage is 80 μm in each of the x, y, and z directions. A dedicated software, developed by our group, translates the structure points to piezo stage positions and controls the synchronization of the movements with the mechanical shutter, in order to achieve the desired local energy dose.

Two different photopolymers have been used for fabrication: the first is a commercial UV curing adhesive (NOA 63, Norland) with optimum sensitivity in the 350–400 nm range, whereas the second is an epoxy-based resin (SU-8, MicroChem). With NOA63, the process starts by depositing a drop of resist on a cover glass and letting it to achieve a mechanical equilibrium followed by a preexposure with a UV lamp done for a few seconds in order to increase the resin viscosity. The SU-8 requires spin coating of the resist on the coverslip, followed by a pre-bake procedure before starting the TPL fabrication.

The laser power (measured before the objective) is set to ~6.5 mW. After exposure of all the point set defining the desired structures, the unpolymerized

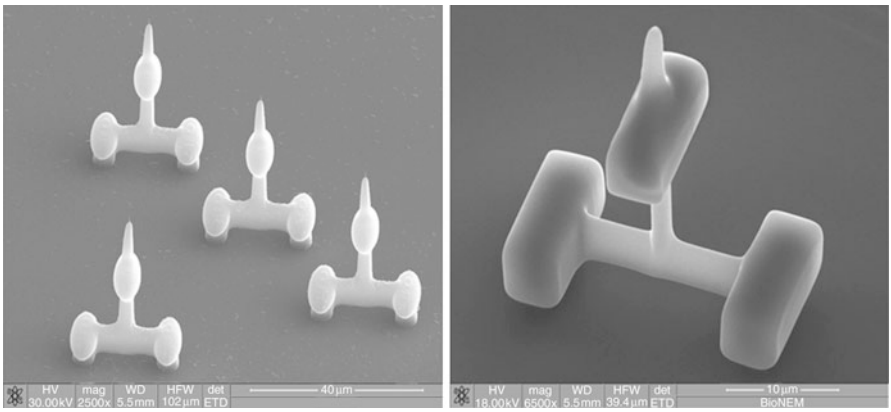

Fig. 19.7 Asymmetrical beads with ellipsoidal (*left*) and with rectangular (*right*) shape of the single composing beads (Picture kindly reprinted from Ref. [47])

resin is removed by developing in acetone for the NOA63 and developing in a proper solvent after a post-bake procedure for the SU-8. In Fig. 19.7, some SU-8 TPL-fabricated beads are shown. The high degree of control of the fabricated structure shape is evident from the ability to choose, e.g., among a rectangular or an ellipsoidal geometry for the single composing beads (see Fig. 19.7).

As a further step, a silver plasmonic nanocone is fabricated on top of the protruding arm, following the procedure described in section 'Microfabrication of Advanced Plasmonic Devices'. Figure 19.8a shows a SEM image of an asymmetrical bead on top of which a nanocone is fabricated.

Afterwards, to enable coupling of the excitation from a focused laser beam into an adiabatic plasmon polariton on the nanocone, a grating is fabricated by using a FIB milling (see section 'Microfabrication of Advanced Plasmonic Devices'). A final fabricated bead is shown in Fig. 19.8b. The presented device was trapped in our OT system, and full 3D manipulation (translation, rotation, and tilting) was successfully tested. The combination of OT and plasmonics could be used for membrane proteins study in living conditions.

Gold Nanocuboid Structures

Metallic nanocubes are intriguing plasmonic nanostructures due to their sharp corners (8 corners, 6 faces, and 12 ridges), where the maximum electric field is localized, and exhibit multipolar resonances [57]. Nanocubes show the focusing of strong plasmon field at the sharp corners and edges, which in turn leads to a dramatic increment in local electromagnetic (EM) field. In the present paragraph, fabrication and characterization of Au plasmonic nanocuboid structures were investigated by means of SERS and numerical simulations.

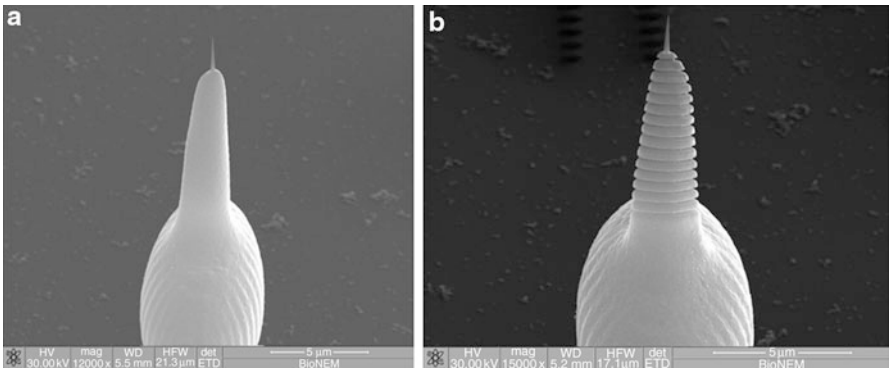

Fig. 19.8 (**a**) Silver nanocone fabricated on the protruding arm of the asymmetrical bead; (**b**) FIB-fabricated grating for plasmonic coupling of the nanocone (Picture kindly reprinted from Ref. [47])

Plasmonic Au nanocuboid structures [58] arranged in the form of 4 × 4 array by varying edge size from 40 to 70 nm with a stepsize of 5 nm were fabricated by electron beam lithography (EBL-Raith 150-Two) associated with lift-off techniques. The height of the nanostructures was fixed to 25 nm. The schematic representation of 4 × 4 array of Au nanocuboid structures with edge size L and interparticle separation (IPS) is represented in Fig. 19.9a. Figure 19.9b represents the typical normal-incidence scanning electron microscope (SEM) image of 4 × 4 array structures with $L = 70$ nm and IPS = 20 nm. Inset represents the magnified view of single nanocuboid structure, which emphasizes the morphological quality in terms of sharp edges and corners.

In order to investigate the effect of Au nanocuboid edge size on SERS intensity, SERS measurements were performed on 4 × 4 array of Au nanocuboid structures with various edge sizes by using Rhodamine-6G (R6G) molecules as analyte. A Renishaw inVia microRaman spectroscopy in backscattering geometry was used to analyze SERS substrate. Thermoelectrically cooled charge-coupled device (CCD) was used as a detector. The spectral resolution of the instrument was 1.1 cm^{-1}. The instrument is equipped with an excitation laser at 633 nm and a 150× objective lens (NA = 0.95) of Leica microscope. The molecules were deposited on to the nanocuboid structures by means of chemisorption technique, in which the nanocuboid substrate was kept in R6G (10 μM) solution for 20 min (which allows the adsorption of R6G molecules to the metal surface) and then taken out and rinsed with deionized water in order to remove excess molecules. After rinsing, the nanocuboid substrate was dried with nitrogen gas and then SERS measurements were performed.

Typical reference Raman spectrum and SERS spectrum of 4 × 4 arrays of 55 nm Au nanocuboid structures are shown in Fig. 19.10a, blue and red trace, respectively. In order to avoid c-Si Raman peak centered at 521 cm^{-1} (first order) and the broad band around 965 cm^{-1} (second order), SERS spectra were acquired in the range of

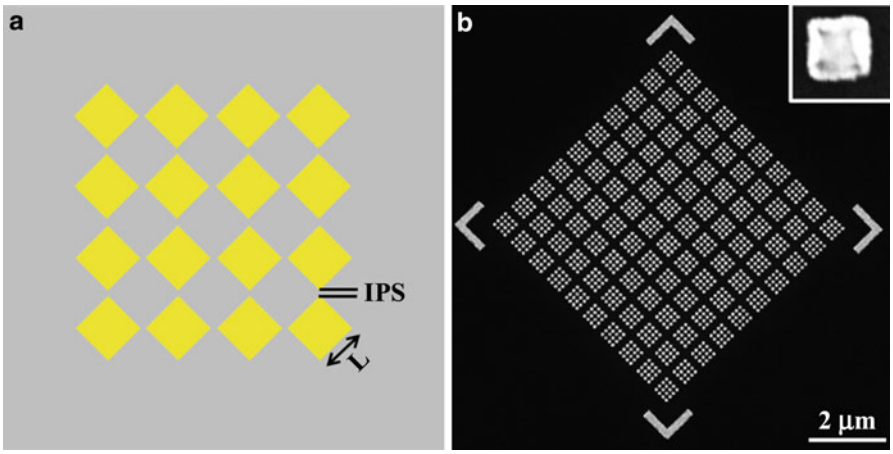

Fig. 19.9 (**a**) Schematic representation of 4 × 4 array of plasmonic Au nanocuboid structures with cuboid edge size *L* and interparticle separation *IPS*. (**b**) Normal-incidence SEM micrograph of 4 × 4 array of 65 nm Au nanocuboid structures with 20 nm IPS. Inset represents the magnified view of single nanocuboid structure (Picture kindly reprinted from Ref. [58])

1,080–1,900 cm^{-1}. The excitation laser power and integration time for reference Raman and SERS spectrum are represented in Fig. 19.10. The incident laser polarization was fixed parallel to the nanocuboid edge. SERS spectrum of R6g molecules on nanocuboid structures (red trace) shows distinct features of R6G. The major bands centered at 1,360, 1,510, and 1,649 cm^{-1} were clearly seen in the spectrum and can be assigned to C–H bending, a combination of C–N stretching, C–H and N–H bending, and combination of ring stretching of the C–C vibration and $C–H_x$ bending of the xanthenes ring, respectively. The peak positions are in good agreement with [44]. Reference Raman spectrum (blue trace) shows the low intense peaks of R6G albeit the laser power and integration time (reported in Fig. 19.10a) were higher than the values used in SERS spectrum of nanocuboid structures. Inset in Fig. 19.10a represents the background Raman spectrum of Au nanocuboid structures taken before chemisorption of R6G molecules. No significant Raman features within the spectral range are observed, thus confirming the absence of surface contamination.

Figure 19.10b represents the variation of SERS intensity with respect to Au nanocuboid size at three different peak positions (1,360, 1,510, and 1,649 cm^{-1}). It is seen that SERS intensity increased with cuboid edge size in the range from 40 to 55 nm and then decreased with rise in cuboid edge size. LSPRs of metal nanoparticle/nanostructure are tunable throughout the visible and near-infrared region of the spectrum by simply acting on the nanoparticle topology [59, 60]. The maximum SERS enhancement can be observed by positioning the LSPR of metal nanostructure close to the excitation wavelength [61, 62]. Therefore, we can assume that the plot observed in Fig. 19.10b corresponds to the resonant

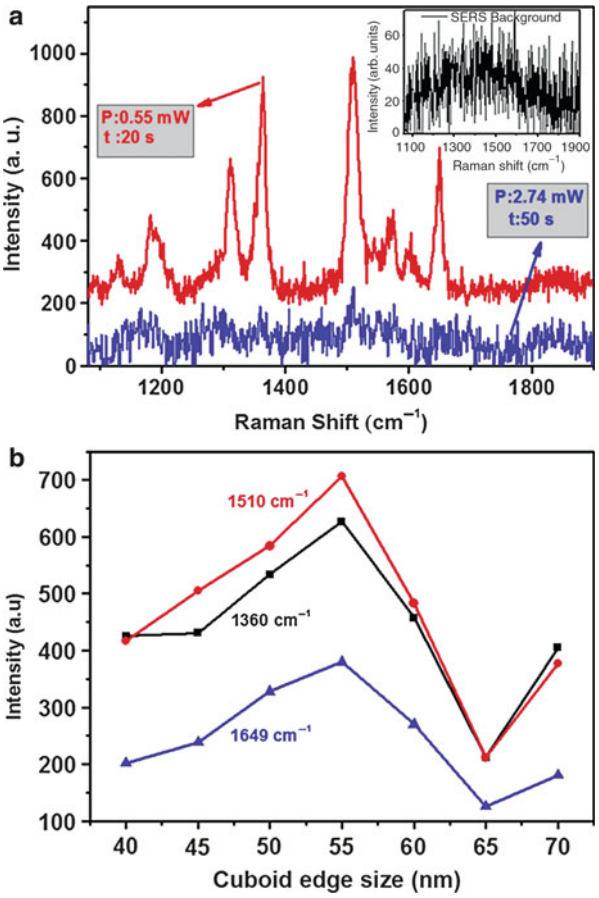

Fig. 19.10 (**a**) Typical reference Raman spectrum and SERS spectrum of 4×4 arrays of 55 nm edge size Au nanocuboid structures after depositing a monolayer of R6G, *blue* and *red* trace, respectively. Inset represents the background Raman spectrum coming from bare 55 nm Au cuboid structures. (**b**) Variation of SERS intensity as a function of cuboid edge size at 1,360, 1,510, and 1,649 cm^{-1} peak positions (Picture kindly reprinted from Ref. [58])

behavior of the nanocuboid structure, centered on $L = 55$ nm. The excitation of LSPR is one of the main mechanisms allowing for signal enhancement in Raman measurements. A similar behavior was observed in the past for nanocylinder structures [63]. SERS enhancement factor was calculated [64] by assuming that the molecules (closely packed) were deposited only on to the metal surface. By considering laser beam focal radius of 500 nm, the average SERS enhancement factor for the reference band centered at 1,510 cm^{-1} is about 10^4 with respect to flat Au marker. The reference band centered at 1,510 cm^{-1} is considered here to calculate the SERS enhancement factor owing to its high signal-to-noise ratio.

In order to understand the electric field distribution in nanocuboid array structures, numerical simulations (CST Microwave Studio) were performed on 4×4 array of Au nanocuboid structures with 55 nm edge size. CST allows the tetrahedral characterization of the geometry, which avoids the generation of fake peaks on curved surfaces. In order to obtain stationary results, convergence mesh analysis was applied. The dielectric constants of Si and Au employed in the present

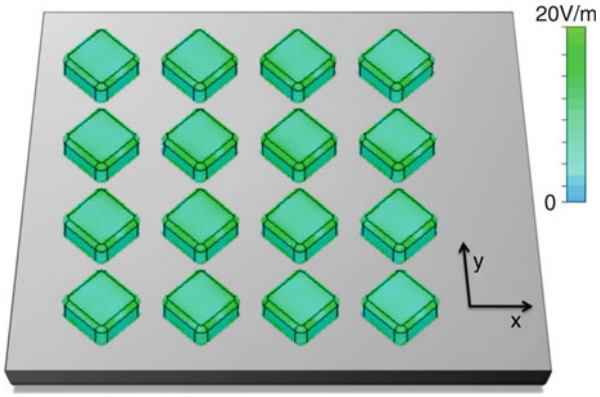

Fig. 19.11 Electric field distribution in *xy* plane with a 633 nm excitation source polarized at 45° with respect to *x*-axis for 4 × 4 array of 55 nm Au cuboid structures (Picture kindly reprinted from Ref. [58])

simulation were $\varepsilon_{Si} = 15.21$ and $\varepsilon_{Au} = -9.79 + 1.97i$ [65], respectively, for $\lambda = 633$ nm. The incident light is polarized along the nanocuboid edge (polarized at 45° with respect to x-axis). Amplitude of the electric field distribution, $|E|$, on the xy plane is shown in Fig. 19.11. The electric field distribution shows a maximum electric field of 20 V/m, localized at the corners of the nanocuboids. By considering the fact that the SERS enhancement is proportional to $|E|^4$ [66], we can conclude that theoretical calculations are supporting experimental results.

Plasmonic Au nanocuboid structures of 4 × 4 arrays with edge size ranging from 40 to 70 nm and with a stepsize of 5 nm were fabricated by EBL technique. Nanocuboid structure size was optimized with SERS by using R6G (10 μM) as analyte. Au nanocuboid structures with 55 nm edge size showed highest SERS intensity. The average SERS enhancement factor of $\sim 10^4$ is observed for 55 nm edge sized cuboid structures with respect to flat Au marker. Au nanocuboid substrate appears as a promising SERS device towards the capability of potential sensitivity for biological and chemical detection even at single-molecule level.

Characterization, Physical, and Chemical Properties of Metal Nanostructures as a Function of the Size, Shape, and Formation Conditions

The Physical Mechanisms of Metal Particles Aggregation at the Nanoscale

While the electroless deposition (see section 'Electroless Metal Deposition') revealed itself effective in forming supramolecular clusters of metal atoms, on the theoretical side the method still lacks an adequate formalization. The aim of this section is to expound on a diffusion-limited aggregation (DLA) model, that is a framework that can describe the aggregation of ions into ordered structures, and give a rationale in the design of devices that utilize rough metal surfaces and effects

thereof, including the very large area of SERS substrates. Moreover, it will be explained how nonconventional variables, including the fractal dimension, can intimately describe the nature of those aggregates with unprecedented accuracy. The new revolution in nanoscience, engineering, and technology is being driven by our ability to manipulate matter at the molecular, nanoparticle, and colloidal level to create designed structures. Using computer simulations and theoretical frameworks, we can discover the fundamental principles of how nanoscale systems behave.

Simulating the Formation of Ordered Superclusters of Metal Atoms

The mechanism of metal growth can be reproduced under the assumption of a diffusion-limited aggregation (DLA) process, where other atomic forces, including steric, electrical, and van der Waals, are instead neglected in the long range limit. This assumption holds true when diffusion dominates over chemical reaction or, equivalently, when the kinetics of metal reduction is extremely fast. The model makes it possible to decipher, at an atomic level, the rules governing the evolution of the growth front and to explore ways to tailor film morphology to obtain specific characteristics [67, 68].

DLA is a simulation method based on simple algorithms that is capable to provide valuable help in understanding natural process, in alternative to models that instead make use of analytical solution of equations [69]. Indeed, in many situations it is possible to model a system by entities that diffuse and occasionally react upon encounter each other. These systems are governed by two time scales: the diffusion time, which is the characteristic time required for two particles to meet, and the reaction time, which is the characteristic time for particles to react when held in proximity (within the reaction range) to each other. When the diffusion time dominates over the reaction time, the process is limited by diffusion. In this case, the immediate neighborhood of a particle is important, because reactions are very likely to take place once particles meet, and the kinetics is dominated by local fluctuations in the distribution of the particles.

DLA is formally regulated by certain rules which can be found, for example, in [67, 70, 71] and are recapitulated below. Proposed for the first time in the pioneering works of Witten and Sander in the early 1980s [67, 71], this numerical framework is very well understood and has been utilized, as for some examples, to reproduce the process of electrodeposition in single wells [72], to investigate the role of sedimentation and buoyancy on the kinetics of colloidal aggregation [73], to describe solute percolation in soils [74], to describe the early stages of thin-film growth at an atomistic scale [68], and to gain insight into physical phenomena including the annealing of defects in crystals [75] and the electron hole recombination [76].

The choice of using here a DLA model where diffusion dominates over chemical reactions is motivated by a number of observations, widely reported in literature, where electroless method produces dendritic nanostructures, with stems, branches, and leaves (Fig. 19.12a) [77, 78]. These fractal structures are generally observed in nonequilibrium growth processes, and DLA is one of the most suitable approaches

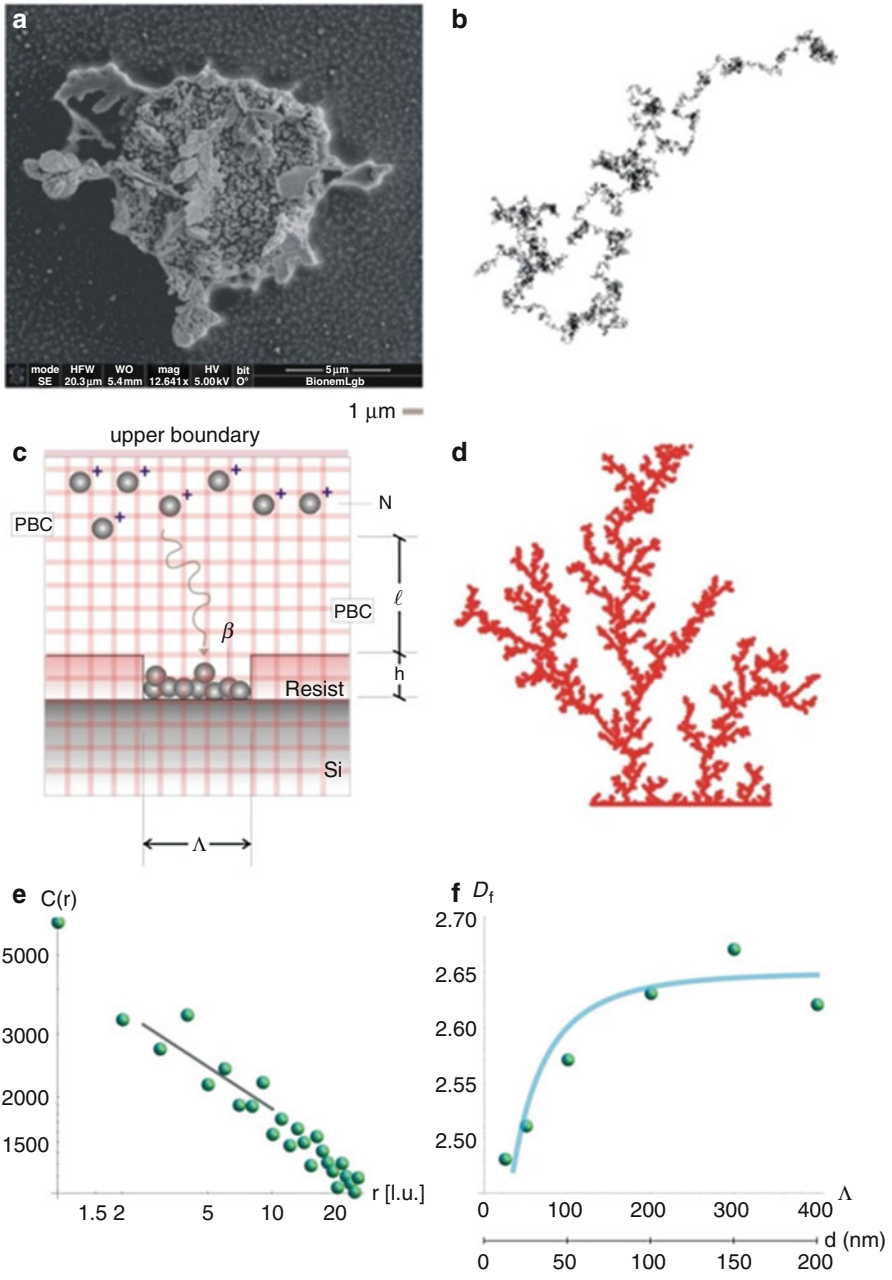

Fig. 19.12 SEM image of a supercluster of silver nanoparticles produced by electroless deposition, revealing a clear dendritic/fractal nature (**a**). Typical pattern of migration of a particle moving a stochastic, random walk: at any step, the probability distribution of the direction of movement is uniform or flat, with events equally likely to occur anywhere within the interval from 0 to 2 π (**b**). Schematic representation of the DLA process reproduced in a regular grid (**c**). The characteristic

for their description. As for an example, Liu and colleagues, while patterning silicon substrates with SERS silver nanograin islands using electroless deposition, observed that the deposition rate could be increased twofold by simply stirring the solution above the substrate, and this would indicate that the overall growth rate is diffusion limited [79]. Moreover, in recent papers describing the process of electroless deposition [32, 78], it is suggested that the formation mechanism of these silver dendritic nanostructures should be considered within the framework of a DLA model. In the model, the displacement of a metal ion, at any time, is arbitrary, and thus, the trajectory of the particles can be correctly described by a random walk, as to resemble a Brownian motion (Fig. 19.12b). Brownian motion is a continuous-time probabilistic process, and its use here is motivated by mathematical convenience and the accuracy of the model to describe an otherwise complex phenomenon. At very short time scales, the motion of a particle undergoing Brownian motion is dominated by its inertia, and its displacement will be linearly dependent on time, $\Delta x = v\ \tau$, and this can be reproduced or simulated in a regular grid (Fig. 19.12c) where particles are dislodged by the finite distance Δx in the time interval τ that is the mean time between collisions. The instantaneous velocity of the particles, v, is maintained constant during τ, and it would depend solely upon the energy of the system. The distribution of displacement probability of the Brownian particle itself is best described using a Gaussian density function, centered around the origin of the walk, that means that the most probable position of a particle after a sufficiently large number of steps is paradoxically its original position. The root mean square distance of the walk gives a measure of the extent of spread of the particle ensemble, and this would be proportional to time [80]:

$$\left\langle r^2 \right\rangle = \left\langle x^2 \right\rangle + \left\langle y^2 \right\rangle = 4Dt \tag{19.8}$$

where x, y, and r are the Cartesian coordinates in the plane, while the celebrated Stokes–Einstein equation may be used to derive the diffusion coefficient D [81]:

$$D = \frac{k_b T}{6\pi\mu a} \tag{19.9}$$

where k_b is the Boltzmann constant, T the absolute temperature of the system, μ the viscosity of the medium, and a is the diameter of a particle with mass m. D can be alternatively expressed in terms of Δx and τ as

Fig. 19.12 (continued) structure generated from the DLA model, the multibranched arrangement of particles recalls the dendrite, fractal nature that electroless grown systems reveal under certain growth conditions (**d**). Power spectrum density function of a numerical aggregate (**e**). The solid line recapitulates the DLA prediction of the fractal dimension of the silver nanoparticle aggregates as a function of pattern size, perfectly matching the experimental points (**f**)

Table 19.2 Physical variables and values thereof of the silver ion gas system considered for the particle growth

Variable	Symbol	Units	Value	Source
Mass of a silver ion	m	[Kg]	1.78×10^{-25}	Ref. [82]
Van der Waals size of a silver ion	R	[m]	$1{,}172 \times 10^{-12}$ m	Ref. [82]
Temperature of the system	T	[k]	323	–
Velocity of the ion	v	[m s^{-1}]	22	$\sqrt{k_b T/m}$
Viscosity of water at T = 323 K	μ	[Pa s]	0.3×10^{-3}	Ref. [82]
Diffusion coefficient	D	[m^2s]	1.5×10^{-9}	$k_b T/6\pi\mu a$
Mean path length	Δx	[nm]	0.5	$4D/v$
Time interval	τ	[s]	2.2×10^{-11}	$\Delta x/v$

$$D = \frac{\Delta x^2}{2\tau} = \frac{(v\,\tau)^2}{2\tau} = \frac{k_b T}{2m} \tag{19.10}$$

where the kinetic theory of gases has been used for obtaining the right-hand term of Eq. 19.10 [80]. Notice that, on comparing Eqs. 19.2 and 19.3, given the results of the simulations, the behavior of the real system would be determined. In the equations above, the time parameter t is an estimate of an hypothetical true external time that a clock measures. The time interval τ can be considered as the simplest basis, or subunit, of this absolute time. An interaction, that is, the dislodgement of a metal ion by a lattice unit, takes the time τ, and the system cannot see or sense any time shorter than τ. To this extent, the total time can be discretized in τ units. τ is not arbitrary and instead depends on physically observable variables of the system, such as the temperature T, the mass m and diameter *a* of the dislodging ions, and the viscosity of the medium. These variables are linked together especially by relations Eqs. 19.2 and 19.10. For the present configuration, those variables assume prescribed values as recapitulated in Table 19.2.

A Case Study: Effect of Pattern Size

This concept was used in [70] to simulate the deposition of metal ions in a patterned silicon substrate, where the size of the pattern was varied over a significant range, namely, from few nanometers to some hundreds of nanometers. Consider, for ease of visualization, the scheme in Fig. 19.12c. At a distance l from the wells, N particles are simultaneously released in the system, where N should be chosen with care to reproduce the initial concentration of silver ions. At any cycle the particles move within a regular square pattern of cells by one lattice unit (l.u.), and thus, the mean path length is Δx = 1 (l.u.). At the side boundaries (i.e., the left and the right) of the domain, periodic boundary conditions (PBC) are imposed, and when an individual particle passes through one of those faces, it instantaneously reappears on the opposite face with the same velocity. In topological terms, the plane can be thought of as being mapped onto a torus; by doing so, an infinite perfect tiling of the system is simulated in the longitudinal direction, and this accounts for the fact that the area of the wells is small compared to the area above the wells. At the upper boundary of

the system, and at the side walls of the wells, a bouncing condition is imposed, whereby the particles which collide with those boundaries would rebound in an opposite direction. After a certain number of repetitions, a particle aggregate is thus formed as in Fig. 19.12d. The multibranched arrangement of particles recalls the dendrite, fractal nature that electroless grown systems reveal under certain growth conditions (Fig. 19.12a). On analyzing the fractal nature of those systems, the fundamental mechanisms of particle aggregation can be revealed. This can be accomplished by deriving the pair correlation function, the power spectrum, and consequently the fractal dimension D_f, of those lattices, as described in the following.

For the present configuration, the parameters of the simulations were adjusted as follows. The simulation was halted after a number of iterations Ni = O (10^{10}). The total number of particles N was held fixed, being N = 2,000.

This numerical procedure was verified against real nanoscale systems. Nanostructures were fabricated via electroless deposition. These comprise clusters or aggregates of silver NPs, clothed in the form of hemispheres, with a diameter ranging from d ~ 20 to d ~ 200 nm (Fig. 19.12f). The structures were imaged using SEM and AFM microscopy. From these profiles, a power spectrum was conveniently derived as described below, and the characteristic fractal dimensions, for each hemisphere, were accordingly determined. These are the mean values derived over multiple measurements and samples, with a small standard deviation, and are reported in the diagram of Fig. 19.12f. Notice that the fractal dimension increases monotonically for increasing d, that is, large structures are less uniform than small ones.

Those results were explained within the realm of DLA theory. The aggregates were produced where the initial seed length Λ is steadily changed from 25 to 400 (l.u.). Considering that, for the present configuration, the mean path length is about $\delta \sim 1/2$ nm the scale factor of the problem is 2, and thus, 25 (l.u.) would roughly correspond to 12.5 nm in the real system and 400 (l.u.) to 200 nm. Per each configuration, a pair correlation analysis was applied (Fig. 19.12e), whereby the fractal dimension D_f of the aggregates was derived. In Fig. 19.12f, the solid line represents the numerical DLA D_f as a function of Λ; in the same diagram, the markers in bright green correspond to the structures produced experimentally. The model recovers the experiments with advanced precision and accuracy and may be used to comprehend and design processes where advanced nanofabrication/characterization techniques are involved.

This DLA framework is *predictive* to the extent that gives the promise of describing the overall dynamics of aggregations of NPs. Specifically, this case study demonstrated that the process of NPs aggregation is size dependent, that is, a remarkable result, and especially, it was found that (i) for small systems, metal aggregates are continuous and homogeneous; (ii) for large systems, metal aggregates are discontinuous and less compact; (iii) the transition from small to large occurs at a size that, for the present configuration, is about d ~ 50 nm; and (iv) for sufficiently large systems, the internal structure of the clusters settles down to a steady state, that is, the growth is constant with d.

Deriving the Fractal Dimension of a Surface

Fractals are mathematical objects that are too irregular to be described by conventional geometry. They all retain, to different extents, certain properties that may be reviewed as follows: (i) they reveal details on arbitrarily small scales (fine structure), (ii) they can be generated (and thus described) by short algorithms (perhaps recursively), and (iii) they exhibit a *fractal* dimension D_f strictly greater than the classical topological dimension [83]. The latter property reserves particular attention, in that it claims that a surface, under a fractal point of view, may have a dimension D_f even greater than 2, and the more D_f is close to 3, the more the fractal set *fills* the space it is embedded in. The fractal dimension of the nanoparticles aggregates can be derived as described below.

Suppose to have an AFM profile of the substrate. This can be thoroughly processed to obtain the corresponding power spectrum density function C(q). C(q) delivers significant information regarding the fractal dimension and microstructure of the substrates at study, it is formally obtained as

$$C_{2D}(q) = \frac{1}{(2\pi)^2}\left(\int \left\langle z(\chi)z(o)e^{-iq\chi}d\chi^2\right\rangle\right) \tag{19.11}$$

where $\chi = (x, y)$ is the planar coordinate; $z(\chi)$ is the surface profile measured from the average surface plane, defined as $<z> = 0$; and q is the wave number, related to the characteristic wavelength λ as $q = 2\pi/\lambda$. The symbol $<\ldots>$ stands for ensemble averaging over a collection of different surfaces with identical statistical properties. Since the 2D power spectrum density introduced above is impractical for comparison purposes, a 1D power spectrum density can be conveniently extracted using the FACA (fractal analysis by circular averaging) approach, as described in [84]. Considering the polar variables q and ψ ($q = (q_x^2 + q_y^2)^{1/2}$; $\psi = \arctan(q_y/q_x)$) in the plane (x, y) of interest, the power spectrum C(q) is derived as an average taken over every circumference Γ of radius q and origin ($q_x = 0$, $q_y = 0$), that is to say,

$$C(q) = \frac{1}{\Gamma}\oint_{\Gamma} C_{2D}(q_x, q_y)d\gamma = \frac{1}{2\pi}\int_0^{2\pi} C_{2D}(q\cos\psi, q\sin\psi)d\psi. \tag{19.12}$$

In the case of self-affine surfaces, for which a rescale in the planar coordinates $x \rightarrow bx$ and $y \rightarrow by$ is accompanied by a rescaling in the normal direction z ($b\boldsymbol{\chi}$)$\rightarrow$ $bHz(\boldsymbol{\chi})$, the power spectrum C(q) takes the form

$$C(q) = \frac{H}{2\pi}\left(\frac{h_o}{q_0}\right)^2\left(\frac{q}{q_0}\right)^{-2(H+1)}, \text{for } q > q_o \tag{19.13}$$

where q_o is the lower cutoff wave number corresponding to an upper cutoff wavelength $\lambda_o = 2\pi/q_o$ and h_o is related to the Rrms roughness amplitude as $h_o = (2)^{1/2}$ Rrms. A self-affine fractal surface can be consequently univocally

identified by specifying the surface roughness (Rrms), the cutoff wave number q_o, and the coefficient H, known as the Hurst coefficient. In a log–log plot, the power spectrum density appears as a line with a slope β for $q > q_o$ (Fig. 19.12e). The slope β is related to the Hurst parameters as $\beta = 2(H + 1)$. The fractal dimension D_f of the surface can be derived from β or H as Df = (8-β)/2 or Df = 3-H. The fractal dimension D_f for a surface ranges from 2, representing a perfectly flat surface (Euclidean dimension of a surface), to 3, representing an extremely rough surface. For $D_f = 2.5$, the so-called Brownian surfaces are identified which have totally random and uncorrelated profiles.

Deriving the Fractal Dimension of a Diffusion-Limited Aggregation (DLA) Aggregate

The structure of clusters of occupied lattice sites (Fig. 19.12d) exhibits geometric scaling relationships which are characteristic of fractals and can be used to estimate an effective fractal dimensionality D_f. The fractal dimension is a parameter that can be used to describe intimately the topography of a variety of systems, especially at the nanoscales. The importance of D_f resides in the fact that it is used in the definition of certain parameters or properties which describe the deposit.

As, for an instance, the thickness T of the aggregate scales with the total number of deposited particles n, as [85]

$$T \sim n^{1/(D_f-1)} \tag{19.14}$$

the fractal dimension is also correlated to the distribution or number I of clusters with size S as a function of cluster size [85]:

$$I(S) \sim S^{-(1+1/D_f)} \tag{19.15}$$

Most importantly, the mean cluster size can be deduced and correlated to n via a very simple power law, being [86]

$$S \sim n^{D_f/(D_f-1)}, \tag{19.16}$$

and thus, given n, that can be easily calculated, the mean cluster size would be readily derived. Similarly to what described for real surfaces in the former paragraph, the fractal dimension of the numerical aggregates can be derived from their characteristic power spectrum density function C(q). Specifically, the power spectrum of a numerical data set can be determined from a pair correlation analysis. The pair correlation function g(r) is related to the probability of finding the center of a particle at a given distance r from the center of another particle. For short distances, this is related to how the particles are packed together. Here, we provide a simple algorithm following which g(r) may be calculated. One should choose and fix a value of dr sufficiently small. Therefore, for all the values of r considered for the analysis, the following steps of a procedure should be repeated: (i) count the

particles positioned at a distance comprised between r and r + dr from the reference particle. Those are all particles in a circular shell, with thickness dr, surrounding the reference particle. (ii) Divide your total count by the number of reference particles you considered. (iii) Divide this number by $2\pi r\,dr$, that is, the area of the circular shell. This accounts for the fact that as r gets larger, for trivial reasons you find more particles with the given separation. (iv) Divide this by the particle number density. This ensures that $g(r) = 1$ for data with no structure. (v) The resulting value is the value of the pair correlation function at the specific distance r, g(r).

DNA Templating on Superhydrophobic Micropillar Surfaces for Nanowire Circuitry

In this section we will discuss the possibility to exploit the peculiar evaporation dynamics of liquid drops on superhydrophobic surfaces to obtain suspended nanowires with diameters below 100 nm and length in the mm range. The idea is the following: the retraction of a liquid droplet loaded with lambda DNA on a superhydrophobic surface consisting of an array of regular micropillars leads to suspended DNA strings or bundles that span regular patterns over the pillars [87]. In the next step, these DNA nanowire templates can be coated with metals, for example, by thermal gold evaporation, to obtain good electrical conductivity, and clever control of the DNA drop motion during drying can be employed to design complex patterns via evaporative self-assembly [88, 89]. Furthermore, optical functionality can be added to the nanowires by growing semiconductor nanocrystals on top of the gold coating, which we will demonstrate with ZnO. Such hybrid metal–semiconductor wires should have interesting properties for photodetection in the UV range, and the suspended nanowire geometry should provide a particularly large surface area for interaction with the environment. In the following we will describe the superhydrophobic surface fabrication, the DNA deposition to obtain the nanowire templates, the metallization, and finally the decoration with ZnO nanocrystals in detail.

The fabrication of the SU-8 micropillars involves a two-step approach composed by (i) an optical lithography phase to define the position of the microstructures and their development and (ii) a plasma process to cover the chip with a Teflon layer to make the surface superhydrophobic and/or to add a nanoroughness on the top of the micropillars to further enhance the non-wetting features and the anchoring of DNA nanowires.

The SU-8 resin contains eight epoxy groups per molecule which gives the polymer very high functionality. The high degree of cross-linking gives it good thermal stability ($Tg > 200\ ^\circ C$). When fully processed, SU-8 creates a glass-like surface that is extremely hard and difficult to remove, which is due to its molecular structure that is formed during the exposure and post-exposure baking (PEB). Fully cross-linked SU-8 forms a ladder or H structure at the molecular level, and it is this repeating chemical chain which gives to the fully cured SU-8 its strength.

The micropillar structure is fabricated by first rinsing a Si wafer acetone, followed by IPA rinse (isopropyl alcohol) and drying with N_2. To remove solvent residues from surface, the wafer is then baked on a hot plate for 5/10 min at a temperature between 85 °C and 105 °C. SU-8 is then spin coated (1,500 RPM per 60 s) on the surface. Before exposure, the Si wafer coated with the SU-8 passes through a soft-baking (65 °C/5 min, 95 °C/40–45 min), which ensures the evaporation of the solvent and the densification of the film. For better results, ramping or stepping the soft bake temperature is performed. Indeed, lower initial bake temperatures allow the solvent to evaporate out of the film in a more controlled way. The following step is the exposure (15 s) during which UV radiation passes through the clear zones of the optical mask. After the exposure the sample is baked again (PEB, post exposure baking 65 °C/5 min, 95 °C/15 min) to selectively cross-link the exposed portions of the film. Finally, the sample is first immersed in a SU-8 developer (10 min), performing strong agitation to obtain high aspect ratio, and finally rinsed in IPA and dried by nitrogen.

The second step involves an ICP-RIE (inductive coupled plasma-reactive ion etch) plasma Teflon coating or a plasma nanotexturing + Teflon coating. In the first case, the sample is processed for 10 s in a plasma environment created by the injection of 85 sccm of C_4F_8 with a chamber pressure of 27 mT and an ICP/RF power of respectively 1 W and 600 W. In the second case, a plasma texturing precedes the Teflon coating and creates a nanoscale fibrillar structure on the top of the pillars enhancing the superhydrophobic features of the substrate. This plasma etch consist of a CF_4/O_2 flux (5/15 sccm) at pressure of 9.06 Pa and an ICP/RF power of respectively 100 W and 50 W for 10 min (Fig. 19.13).

The fabrication of ordered 1D organic nanostructures on a large scale is a challenging subject that holds promising spin-off in next generation high performance optoelectronic devices [90, 91]. Here, we show how ordered hexagonal arrays of SU-8 pillars with superhydrophobic behavior and three-phase wetting were exploited to obtain regular and controlled DNA wire arrays. Such surfaces allow the fine control of wire diameters and length by controlling the overall wetting behavior and the local surface–molecule–solvent interaction [92], in terms of shear viscosity and interaction time.

Double strand λ-DNA has been suspended in phosphate buffer solution (PBS) (50 ng/μl DNA in 1 % PBS volume). A drop of 4–7 μl has been deposited onto the superhydrophobic pillar surface, fabricated as above described. A three-phase contact (TPC) line was created, and a suitable contact time was chosen in order to trigger a gravity-driven DNA concentration gradient within the drop. This procedure allows the DNA molecule to get in contact and interact with the wetted features of the surface (top of the pillars). Once the wetting interface is created, the drop can be let to evaporate overnight [93]: in this process, the solvent evaporation induces changes in the drop/substrate wetting condition, which leads to a sequence of pinning and depinning processes from the pillars [87, 94]. Alternatively, a similar pinning/depinning process can be obtained by relative motion of the substrate with respect to the DNA solution droplet, which sensibly influences the shear flow conditions during the shrinking of the drop as reported by us previously [95].

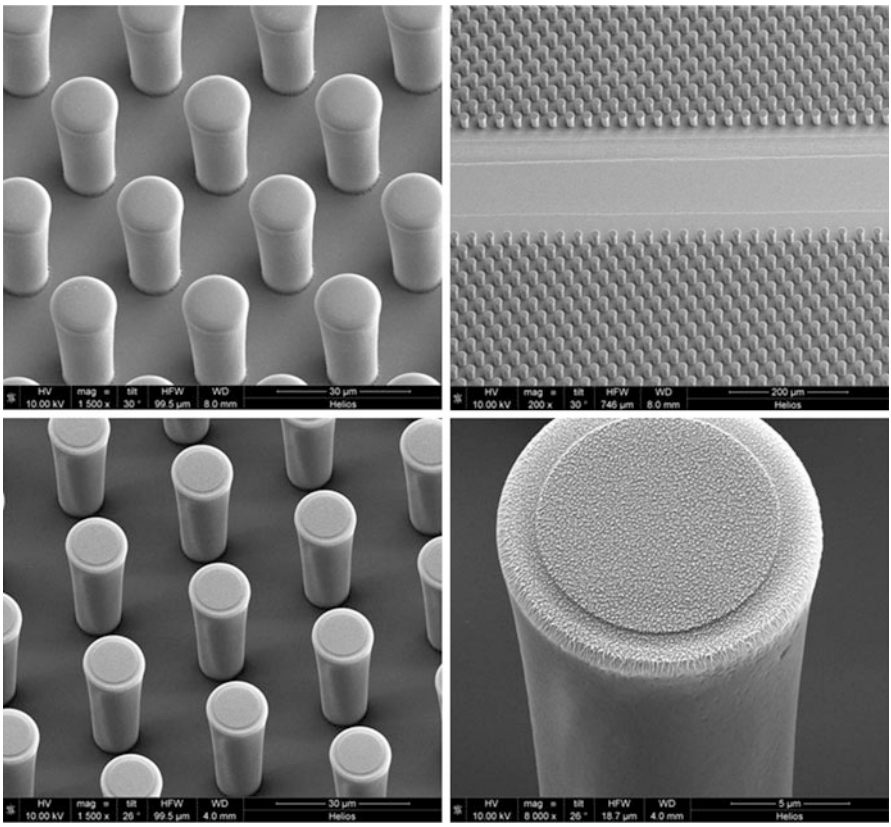

Fig. 19.13 SEM images of SU-8 micropillar arrays without (*up*) and with (*down*) the plasma nanotexturing on top

This dynamic process is similar to Langmuir–Blodgett preparation: once a tip was linked to the drop, a relative tangential motion was applied at the TPC with a velocity comprised between 100 and 600 um/s. While moving the drop/support contact line, DNA molecules were stretched and suspended between the pin points of the surface, i.e., the wetting features. The process yields an ordered and tunable array of 1D organic nanostructures consisting in DNA bundles. The forces responsible for the formation of the bundles were basically the capillary force F_c and the pulling force F_p necessary to pull a DNA molecule or bundles [87]. Capillary force involves surface tension at the contact line and liquid viscosity. Tuning the velocity it was possible to achieve a desired pulling force, thus selecting the diameters of DNA bundle to be stretched (Fig. 19.14).

Furthermore, the tuning of the direction of the TPC motion allows the fabrication of organic meshes and grids in a few simple steps (Fig. 19.15).

DNA bundles can serve as an optimal template for the cost-effective nanowire fabrication with large area coverage. The obtained 1D structures can be coated with

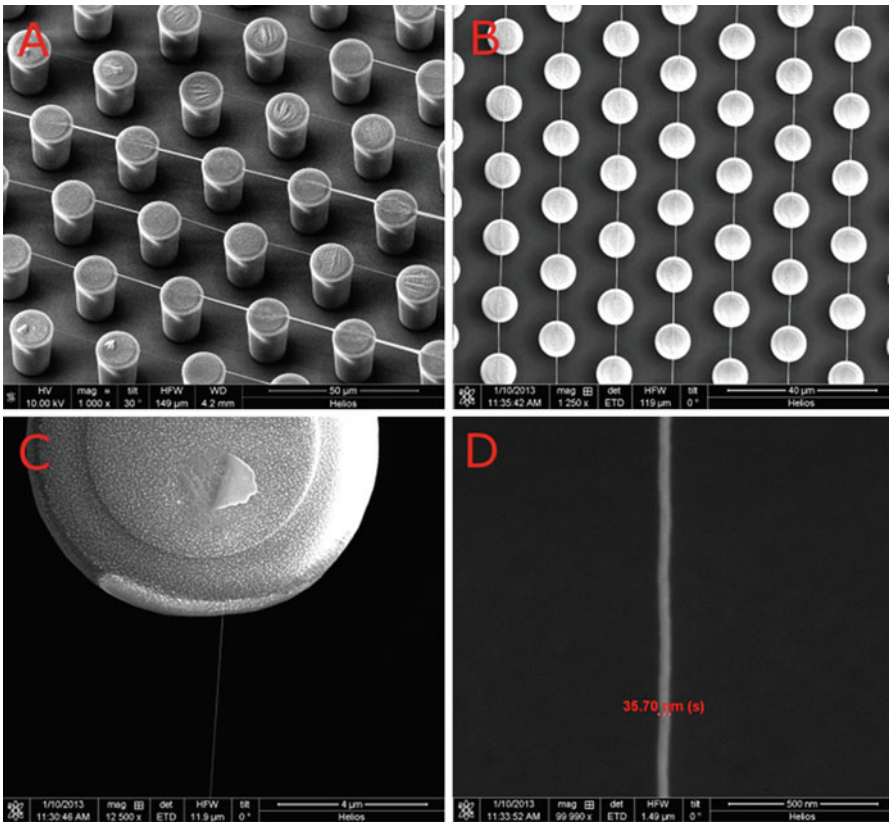

Fig. 19.14 SEM images of DNA filaments stretched and suspended on SU-8 micropillars. In (**a**) and (**b**), an overview of the surface and 1D DNA directional arrays is shown. In (**c**) and (**d**), a detail of the filament diameters is shown

metals by means of thermal evaporation resulting in conducting wires with controlled diameter that are suspended on an insulating pillar arrays with tailored periodicity and wire meshes. Such suspended nanowire networks are particularly attractive for sensing applications due to the large exposed surface area.

As proof of concept, we have deposited 30 nm of Au onto the above described nanowire templates by thermal evaporation. We used pillar structures with undercut lateral profiles to avoid electrical shortcuts between the electrical circuitry and the bottom of the substrate. We have performed electrical characterization of the suspended nanowires in between individual pillars by contacting neighboring pillars with tungsten micromanipulators (tip radius 5 µm). Typical current–voltage curves of a suspended Au-coated DNA nanowire with around 100 nm diameter suspended between pillars with 18 µm distance are shown in Fig. 19.16. At low bias, we observe ohmic behavior (red solid line in Fig. 19.16), as expected. If the bias voltage is increased to some hundreds of mV, the current gets into saturation

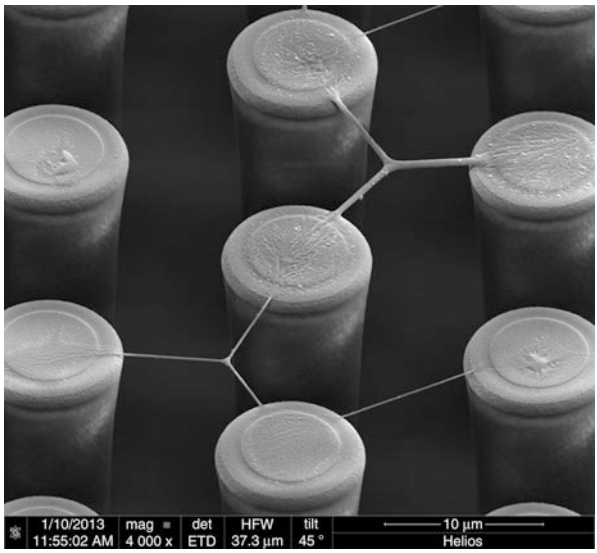

Fig. 19.15 SEM image of λ-DNA meshes obtained by crossing different TPC lines by support/drop motion

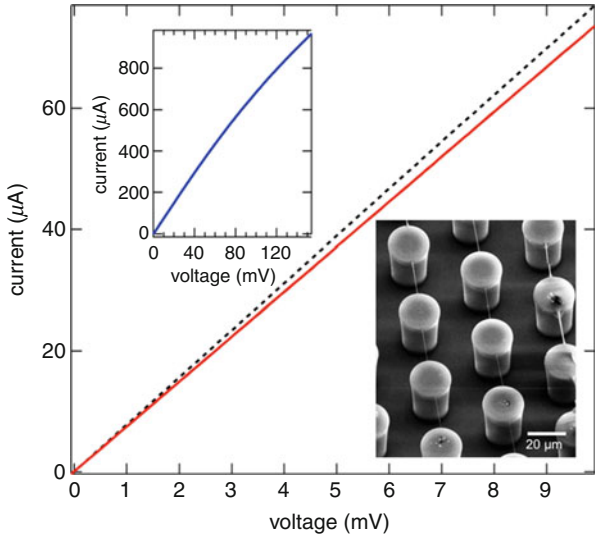

Fig. 19.16 Current–voltage curves of a suspended Au-coated DNA wire measured between two adjacent pillars: first, the solid red curve in a low bias regime was recorded, then the bias was increased until current saturation set in (*upper inset*), and after this, the IV was recorded again at low bias (*dashed black curve*), showing increased conductivity. The SEM image in the inset shows the Au-coated wires under test. The distance in between the pillars was 18 µm

(upper inset), and upon further increase it will be burned [96]. The current saturation can be understood by nanowire heating due to the high current density (of the order of 10^8 A/cm^2). Interestingly, the nanowires demonstrate higher conductivity after being ramped into saturation as shown by the dashed line in Fig. 19.16. This can be rationalized by the annealing effect caused by the high current density that should lead to a more homogeneous Au film.

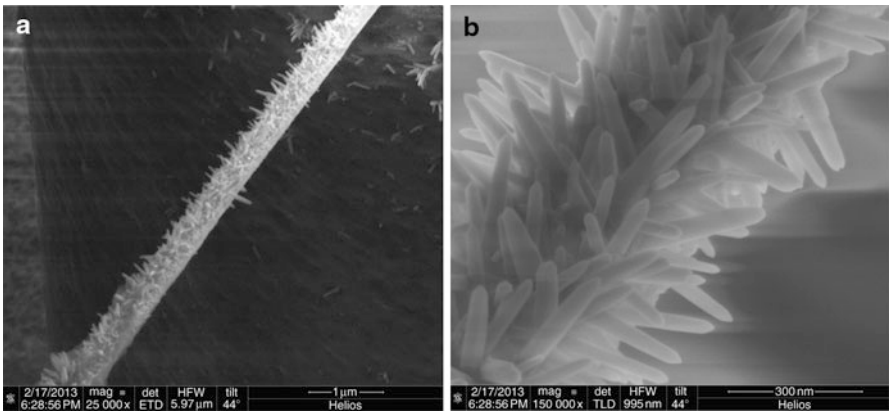

Fig. 19.17 ZnO nanocrystals hydrothermally grown on DNA bundles (**a**). In (**b**) a detail of radial symmetric ZnO nanocrystal growth is shown

Eventually, the nanowire templates can be decorated with other nanomaterials that have different functionality, or they can act as templates for nanocrystal growth. This approach opens new pathways for the fabrication of hybrid nanowire architectures for novel device applications, for example, optical sensors that could work in liquid environment.

In order to demonstrate the feasibility of this approach, we have used the Au-coated DNA nanowires as templates for zinc oxide (ZnO) crystals hydrothermal growth [97–99]. Figure 19.17 shows sections of such ZnO-decorated nanowires, evidencing that the ZnO grows in rodlike structures in radial direction, instead of a homogeneous layer. This spinose decoration results in an extremely high surface area that can be useful for sensing applications. In detail, we deposited a thin (20 nm) ZnO film by thermal evaporation on a chip with Au-coated DNA bundles in order to create a seed layer. Then, the sample containing the suspended Au–ZnO DNA wires was immersed in an aqueous solution of ZnO precursors (zinc nitrate, $Zn(NO_3)_2$ $6H_2O$ 25 mM; hexamethylenetetramine, (HTMA) 25 mM; and poly(ethyleneimine), (PEI) 6 mM) and kept at 90 °C for 40 min. Afterwards, the support was washed several times with DI water and gently blow-dried with nitrogen.

The obtained hybrid ZnO–Au (metal semiconductor) can be expected to show photocurrent when excited with laser light above the band gap of ZnO, thus in the UV spectral region. Here, the Au core should facilitate good electrical conduction, while the ZnO acts as the light-absorbing material. Furthermore, this hybrid architecture with very large ZnO surface area can also be interesting in solar cell applications in combination with a hole harvesting polymer matrix.

Properties, Specific Physical Effects of Metal Nanostructures, and the Case of Surface Plasmon Resonance

L-Shape Gap Nanoantenna Dimers Supporting Plasmon-Polariton Modes

The most remarkable property of plasmonic nanostructures consists in the easy coupling between electromagnetic (EM) radiation and *surface plasmon polaritons* (SPPs) [100]. In particular, when the dimensions of the systems under study are shorter than the incoming radiation wavelength, the quasi-static approximation well describes EM responses and the plasmonic modes supported by the structures can be defined as *localized surface plasmons* (LSPs) [101].

Sub-wavelength nanoantennas are typical nanostructure devices able to efficiently convert free propagating EM radiation into near-field EM energy, concentrated into sub-wavelength active regions called *hot spots* [102]. Such property, in visible (VIS) and near-infrared (NIR) spectral region, can be efficiently exploited for advanced spectroscopic techniques with particular applications in biosensing and biomolecular spectroscopy, in perspective to achieve the challenging single-molecule detection [103, 104]. In order to obtain an antenna-based device able to efficiently couple to light, generating an intense and localized hot spot, an optimal solution consists in putting two nanoantennas in close proximity [20].

When two sub-wavelength plasmonic nanostructures exposed to EM radiation are put at a mutual distance shorter than their typical dimensions, a strong overlapping occurs between their generated near-field *evanescent tails* [105]. In this condition, in analogy to the theory of molecular orbitals, Maxwell's equations admit for the coupled system two hybridized eigenmodes which result from the interaction between the unperturbed LSP modes supported by each nanostructure. The energies associated to such modes are respectively lower and higher than the degenerate energy level, and the difference between them depends upon the intensity of the interaction. The lower energy plasmonic mode is defined as *bonding* while the higher one is called *antibonding* [106].

By arranging nanoantenna dimers in an L-shape gap configuration (see Fig. 19.18a), it is possible to obtain a device supporting plasmon-polariton modes that are combinations of in-phase (bonding mode) and out-of-phase (antibonding mode) single antenna long-axis surface plasma oscillations. In the former case, charge distributions induce in the gap region an intense hot spot while in the latter one a 'zero-field spot' occurs in a plasmonic mode which can be referred to a nonzero dipolar momentum [107].

The crucial point on which the EM behavior of L-shape antennas device consists in the strong gap-induced coupling between the LSPs supported by each nanoantenna arm. Considering the VIS–NIR spectral region as working range of the device, the gaps between the apexes of antenna arms have to be around 10 nm in order to show appreciable hybridization of plasmonic states. In such perspective, the technique employed for the realization of L-shape antennas device has been *electron beam lithography* (EBL), a fabrication approach particularly addressed for

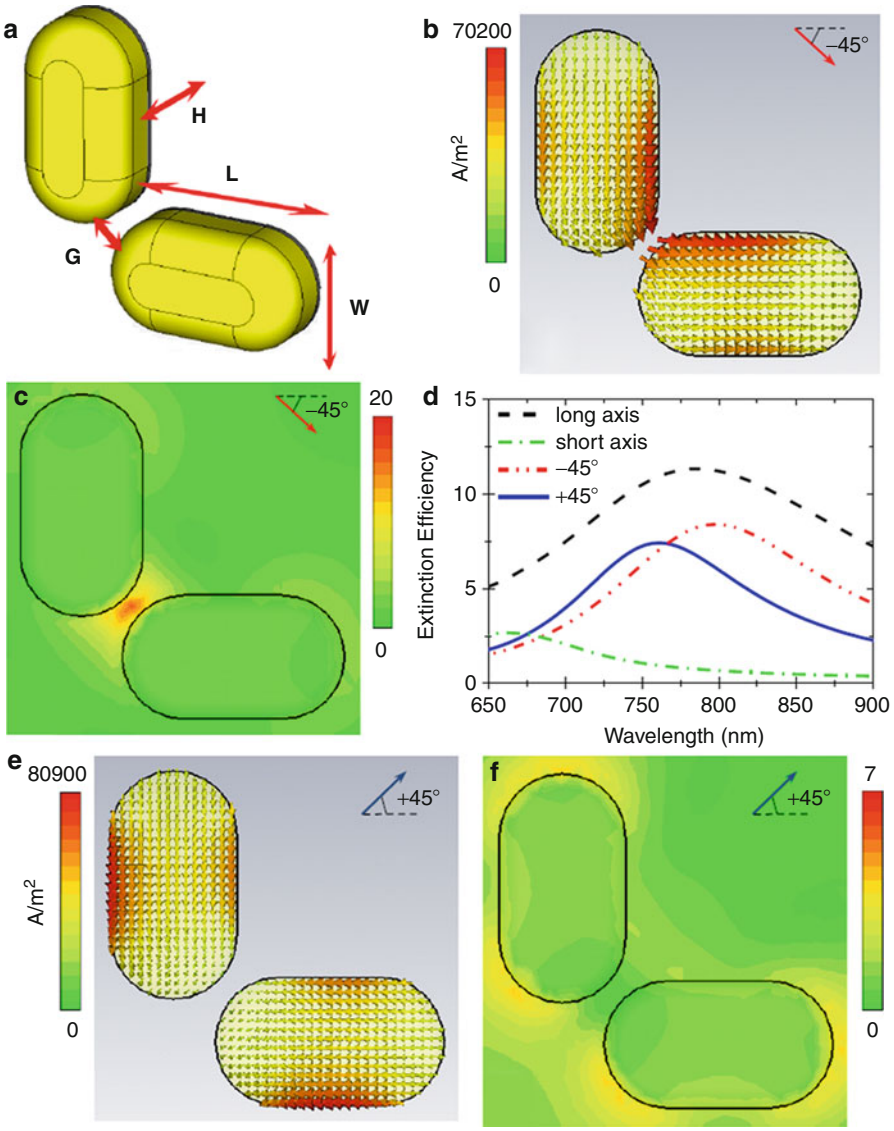

Fig. 19.18 (**a**) 3D sketch of L-shape antennas showing the geometrical parameters representative of the morphology (**b**, **c**) Respectively, current density and electric field intensity 2D plots for normal-incidence light polarized at -45° valued at $\lambda = 810$ nm (**d**) Theoretical extinction efficiency spectra of L-shape antennas ($L = 190$ nm, $W = 110$ nm, $H = 60$ nm, and $G = 20$ nm) and of their single antenna arm; in *black dashed line* the long-axis reference extinction spectrum of single antenna, in *green dotted/dashed line* the short-axis reference extinction spectrum of single antenna, in red double-dotted/dashed line the L-shape antenna extinction spectrum for -45° polarization, and in blue continuous line the L-shape antenna extinction spectrum for $+45^\circ$ polarization (**e**, **f**) Respectively, current density and electric field intensity 2D plots for normal-incidence light polarized at $+45^\circ$ valued at $\lambda = 760$ nm (Picture kindly reprinted from Ref. [107])

the achievement of high nanostructure accuracy and reproducibility over large areas (order of the mm^2). Such procedure involves several steps. Initially, a positive electronic resist (*polymethylmethacrylate* – PMMA) is spin coated on a CaF_2 (100) substrate, chosen for its high transparency in VIS–NIR spectral region. Afterwards, a thin Al layer is evaporated on the resist in perspective of preventing electron charging effects during the exposure process. Once the Al-coated resist layer has been prepared, the sample is exposed to an electronic beam accelerated to 20 KeV. Therefore, after the Al removal in KOH, the patterned resist is developed in a conventional MIBK/IPA solution in order to produce a positive mask. Hence, *physical vapor deposition* (PVD) at room temperature, respectively of 5 nm Ti as adhesion layer and 55 nm Au, is performed on the sample. Finally, the unexposed resist is removed with acetone and rinsed out in IPA. As result of the fabrication process, 40×40 μm^2 size matrices of L-shape antennas have been obtained with interparticle gaps equal to 20 nm (Fig. 19.19a–c).

In quasi-static approximation, L-shape nanoantennas support two pairs of hybridized long-axis LSP modes. In the former mode, charge distributions in both antenna arms flow in-phase in a convenient energetic configuration (Fig. 19.18b). Conversely, the latter mode presents charge distributions forced to contemporarily converge towards the gap in an inconvenient energetic configuration (Fig. 19.18e). As a consequence of that, moving from the bonding to the antibonding mode, the electric field generated within the gap region experiences a strong variation. In fact, from an intense hot spot occurring for the in-phase charges configuration, it is possible to see how the electric field appears completely nullified in the out-of-phase condition (Fig. 19.18c, f). Such two modes are both associable to nonzero dipolar momenta, whose orientations correspond to the lines forming angles respectively $\theta = -45°$ and $\theta = +45°$ with the horizontal antenna long axis. This fact implies that such modes are both able to efficiently couple to light, reemitting EM radiation in far-field. In particular, for incoming light polarized at $\theta = -45°$, it is possible to promote the bonding mode, activating the gap-induced hot spot in near-field and observing a correspondent single broad resonance peak in the extinction efficiency spectrum (red dashed/double-dotted curve in Fig. 19.18d). To the contrary, by rotating the polarization vector of a 90° angle ($\theta = +45°$), it is possible to suppress the bonding mode and consequently the hot spot in the gap region. In this way only the antibonding mode can be excited and observed in far-field as a broad resonance peak centered on a wavelength which is blue-shifted with respect to the bonding wavelength (blue continue curve in Fig. 19.18d).

As it is possible to verify in the extinction efficiency spectra reported in Fig. 19.18d, the peaks observed for L-shape antennas response at $\theta = \pm 45°$ are definitely not related to single antenna short-axis LSPs, which instead occur in a different spectral region (green dashed/dotted curve in Fig. 19.18d), but conversely they result from the hybridization of single antenna long-axis LSPs (black dashed curve in Fig. 19.18d).

Such behavior has been verified by transmission spectroscopy for light polarized at $\theta = -45°$ and $\theta = +45°$, keeping in mind the relation between transmission and extinction efficiency:

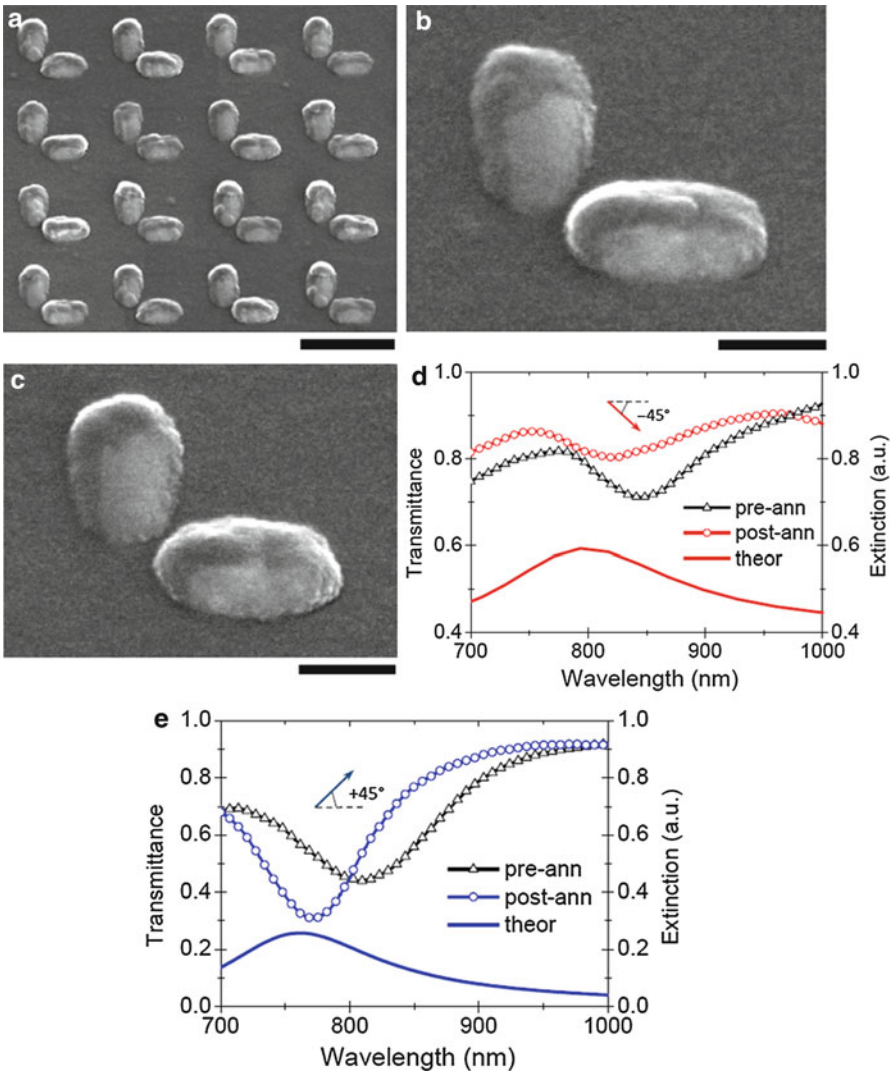

Fig. 19.19 (**a**) and (**b**) Representative SEM images, respectively, of 30° out-of-normal tilted L-shape antenna arrays and single L-shape antenna fabricated by EBL technique before annealing process (scale bars corresponding, respectively, to 400 and 100 nm). The nanostructure geometrical parameters are $L = 190$ nm, $W = 110$ nm, $H = 60$ nm, $G = 20$ nm, and $S = 100$ nm (**c**) Representative SEM image of 30° out-of-normal tilted L-shape antenna after 200 °C annealing (scale bar corresponding to 100 nm) (**d**) Transmission optical spectra of the L-shape antenna arrays before (*black curve with triangles*) and after annealing at 200 °C (*red curve with circles*) and theoretical extinction efficiency (*continuous red curve*) for normal-incidence light polarized at $-45°$ (**e**) Transmission optical spectra of the L-shape antenna arrays before (*black curve with triangles*) and after annealing at 200 °C (*blue curve with circles*) and theoretical extinction efficiency (*continuous blue curve*) for normal-incidence light polarized at $+45°$ (Picture kindly reprinted from Ref. [107])

$$Q_{ext} = \frac{A(1 - T_{rel})}{Na} \tag{19.17}$$

where 'A' is the area illuminated by the light spot, 'N' is the number of arrays elements inside of the spot, and 'a' is the area of L-shaped antenna projection on the plane where the polarization vector lies.

From a comparison between collected and calculated spectra, it is possible to find a good accordance, apart from a slight red-shift of measured resonance wavelengths with respect to theoretical ones (Fig. 19.19d, e). This fact suggests that the hybridization model, which determines the antibonding/bonding energy splitting, is correct even if applied to a system that is not ideal. In fact, as exhaustively described in literature [108], gold aggregates evaporated at room temperature present a nonuniform internal structure. They are organized in grains of about 30 nm size, mainly (111)-oriented, and electrons flowing through them experience multi-scattering effects that result in an additional contribution to their internal damping. More precisely, the damping factor of a gold polycrystalline nanostructure differs from the model system of the following quantity:

$$\Delta\Gamma = \Gamma_g - \Gamma_0 = \frac{1.37 v_F R}{D(1 - R)} \approx \frac{1}{D} \tag{19.18}$$

where 'v_F' is the Fermi velocity for gold, 'R' is the reflection coefficient of electron at the grain boundary, and 'D' is the average diameter of the grains.

Gold atoms within a polycrystalline aggregate at room temperature are 'frozen' in a metastable energetic configuration where the majority of them are organized in grains with an energetically convenient orientation, that is (111), and the remaining ones belong to grains with different orientations. Starting from such configuration and increasing the temperature, it is possible to make the (111)-oriented grains grow at the expense of the other grains, promoting an average grain growth and grain boundary migration. As confirmed by means of X-ray diffraction experiments (reported in [108]), which show the increasing of (111) peak both in intensity and sharpness as function of the *annealing* temperature, the average diameter of the grains increases from 30 nm at room temperature to 40 nm at 400 °C [108]. Therefore, from Eq. 19.2 it is possible to deduce how annealing process on polycrystalline gold aggregates makes the damping factor tend to the theoretically expected value. Finally, the reduction of the damping factor determines a general blue-shift in the LSP resonance (LSPR) wavelength and the shrinking of the resonance peak in the far-field spectrum.

In order to confirm such interpretation of the phenomenon involved, annealing has been performed on L-shape antennas at 200 °C observing a blue-shift of both the in-phase and out-of-phase resonances. The after-annealing transmission spectra collected and reported in Fig. 19.19d, e are in very good accordance with theoretical extinction spectra reconfirming the extra damping factor, introduced by the polycrystalline nature of the structures, as the origin of the resonances mismatch observed at room temperature.

Adiabatic Cones, Photonic Crystals, and Superhydrophobicity: A Versatile Tool for Chemical Mapping and Single-Molecule Detection

The main interest in the fabrication of nanoscaled tapered waveguides, such as metallic nanocones, is due to the fact that this kind of structures is predicted [109] and can actually [3] focus and concentrate the optical radiation energy at the nanometric scale. This phenomenon is of paramount importance since it offers the possibility to overcome the diffraction limit of light, and optical-based techniques, like Raman spectroscopy, can exploit this mechanism to achieve an unprecedented spatial resolution. This focusing effect can be achieved by excitation of surface plasmon polaritons propagating towards the tip of a tapered metal nanowaveguide, and, with proper geometric conditions, the surface plasmon polaritons adiabatically slow down and simultaneously increase the accompanying electromagnetic field.

Microfabrication of Advanced Plasmonic Devices

It is a crucial point that the nano-waveguide is properly shaped as a cone with an accurate control of the apex angle and of the curvature radius of the final tip.

These requirements make the standard micro- and nanofabrication techniques with top-down approach, such as the lithographic techniques, not suitable for the fabrication of these devices. In fact, lithographic techniques, for example, electron beam lithography (EBL), have the capability to achieve the necessary spatial resolution, but they are intrinsically 2D (two-dimensional) processes and not well suited for the 3D structures here required. In EBL processes, typically a 2D pattern is prepared with some CAD software and then replicated on a resist layer by means of a spatially selected electron beam exposure of the resist. After resist development, the 2D resist pattern is transferred to the substrate through an additive or subtractive process. In the additive process, some material, e.g., a thin metal layer, is deposited on the sample, and the final result is a 2D metal pattern; in the subtractive process, the resist pattern is used as a mask through which the material from the substrate is removed by means of an etching step, thus producing a 2D pattern in the material of the substrate (typically a Si substrate or similar). So the only 3D feature of this process is a 2D pattern with vertical walls. Such an approach makes very difficult to produce real 3D structures [110, 111], in which something more than a vertical wall is required. Even simple 3D solids, like a cone or a pyramid, is not a trivial task with standard lithographic techniques, and more in general whenever a tilted, bent, or curved shape is required the intrinsically 2D nanofabrication meets strong limitations.

In order to overcome these troubles, different nanofabrication techniques have to be pursued beside the standard 2D lithographic processes. More in detail, electron beam-induced deposition (EBID) combined with focused ion beam milling (FIBM) is exploited in the present case to produce metal cone-shaped nanodevices coupled to a photonic crystal (PC) optical cavity (Fig. 19.20).

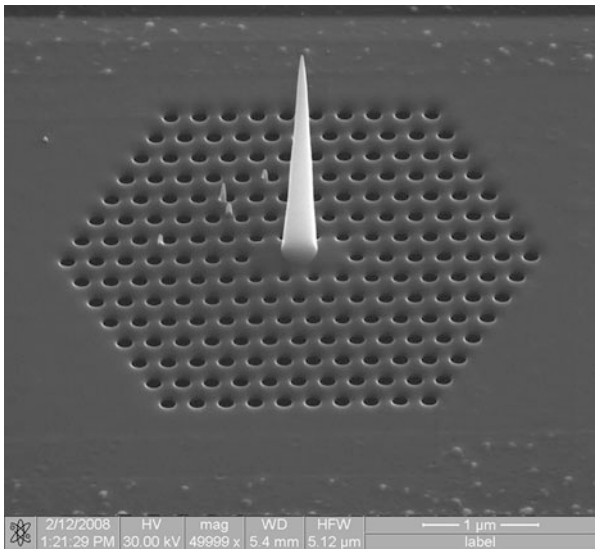

Fig. 19.20 Photonic crystal array and cavity with metallic cone-shaped nano-waveguide in the middle of the cavity. The substrate is a 100 nm thick Si_3N_4 membrane in which air holes are produced by means of ion beam lithography (*IBL*). The nanocone is produced by means of electron beam-induced deposition (*EBID*) technique and is made of platinum carbon covered with an Ag thin layer (20 nm) (Picture kindly reprinted from cover page of Nature Nanotechnology (2010) [3])

The working principle of FIBM is the same as EBL, but in this case, an ion beam is used instead of an electron beam. For the fabrication of this device, Ga^+ ions with an accelerating voltage of 30 kV are used to produce air holes in a thin Si_3N_4 membrane. So the Ga^+ ion beam is exploited to produce a real milling of the substrate with material removal. This effect is produced by physical bombardment of the substrate by the 'heavy' ions. In comparison, the 'light' electrons of EBL do not produce any milling effect but only destroy some molecular bonds in the polymeric chains of the resist, thus changing locally the chemical properties (such as the dissolution rate in presence of solvents) of the resist layer. The similarity of FIBM with EBL is that both the techniques are 2D fabrication processes in which a charged particle beam (ions or electrons) is focused on the sample surface and deflected over the sample in agreement with a CAD designed pattern. The difference is that in EBL, the 2D pattern reproduces a 2D change of the chemical properties of the resist, while in FIBM, in the present case of the device of Fig. 19.20, we use the Ga^+ ions to physically remove material from the substrate in agreement with the 2D pattern. This is made possible by the fact that the thickness of the Si_3N_4 substrate is a small one, in the 100 nm regime. The array of air holes produced in the substrate constitutes a photonic crystal [112, 113], and the three missing holes in the center of the array (where the base of the cone is placed) realize a photonic crystal optical cavity [114], termed L3. The whole array has triangular lattice geometry with lattice constant of 250 nm (Fig. 19.21) and the holes have 160 nm diameter size; these geometrical features make the PC and cavity tuned at a laser wavelength of $\lambda = 532$ nm.

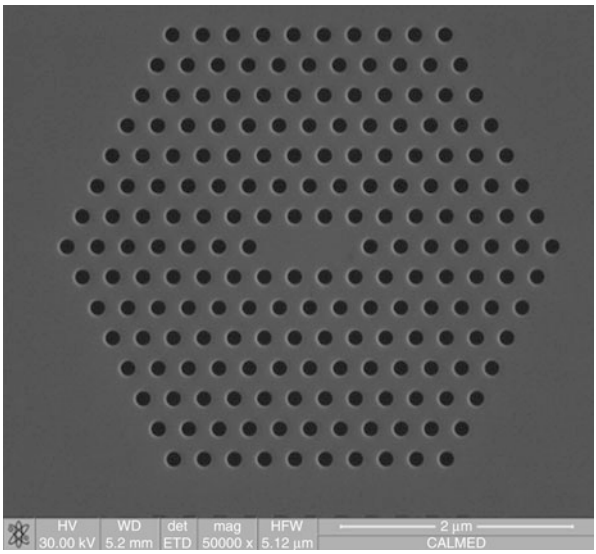

Fig. 19.21 Si_3N_4 photonic crystal: the lattice of the air holes is a triangular one with lattice constant of 250 nm; the holes diameter is 160 nm. The thickness of the Si_3N_4 membrane is 100 nm

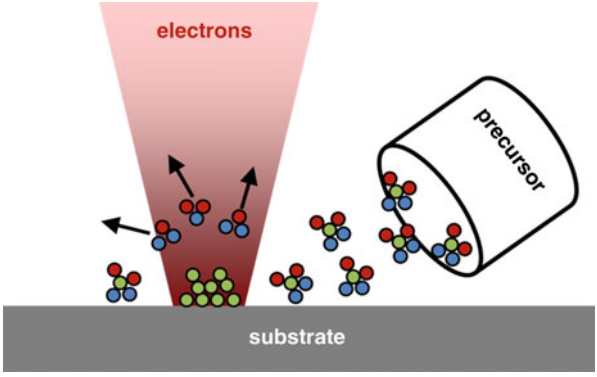

Fig. 19.22 Schematic representation of the electron beam-induced deposition (EBID). $(CH_3)_3Pt(CpCH_3)$ molecules of the precursor gas are broken thus allowing for Pt deposition on the substrate

So far the employed technique is still a 2D fabrication process. The real 3D process is the fabrication of the cone-shaped nano-waveguide in the center of the PC structure. In order to achieve the result of Fig. 19.20, an EBID process is exploited. Electron beam-induced deposition [115] is a structuring technique capable of the same high spatial resolution typical of electron beam techniques, but with the advantage of some 3D capabilities. In EBID (Fig. 19.22), a gas of precursor molecules, in this case $(CH_3)_3Pt(CpCH_3)$ (methylcyclo-pentadienyltrimethyl-platinum), is injected in the vacuum chamber in the proximity of the substrate surface.

The electron beam is focused on the same substrate, in the area where the gas is injected, and hits the molecules of the precursor gas. This bombardment causes the precursor molecules to be broken in more fragments and to release the Pt atom that soon is deposited on the substrate; the other fragments of the molecules are instead

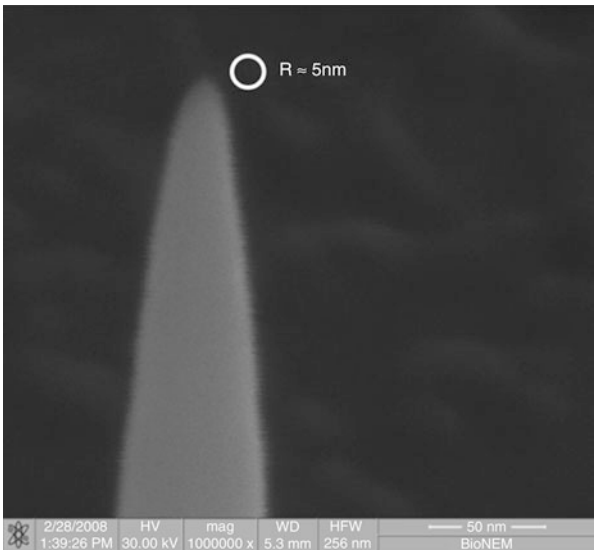

Fig. 19.23 Detailed view of the tip apex, with a curvature radius of about 5 nm (Picture kindly rearranged from Ref [3])

volatile ones and are pumped away by the vacuum system. The only disadvantage of this mechanism is that the Pt deposition so induced is not of pure Pt, but carbon is also deposited to a certain amount on the substrate. The Pt–C material deposited is however a metallic one, since it is conductive both electrically and thermally. This disadvantage mainly comes from the fact that the precursor molecules so far used in EBID techniques are metallorganic materials. The minimum size of the deposited material is comparable with the spot-size of the electron beam, thus being in the more advanced equipments in the 10 nm range. The thickness of the deposited material depends on the dwell time the electron beam is kept in a fixed position on the substrate. So it is possible to deposit a first layer of Pt–C with a desired 2D shape and subsequently to deposit the next layer starting from the previous one but with a different 2D shape. The reiteration of this process allows for an easy fabrication of 3D structures. As a simple example, the cone-shaped nano-waveguides have been fabricated as a vertical stack of disks with different diameters, starting from the largest disk deposited directly on the Si_3N_4 substrate and going on with the smaller disks deposited on the former ones. The process has been reiterated starting from a disk with 300 nm diameter which constitutes the base of the cone and going up towards smaller and smaller disks, till the last one which is constituted by a single pixel and so ensures the smallest curvature radius at the tip apex (Fig. 19.23).

The final height of the cone is imposed to be 2.5 μm for geometrical reasons due to surface plasmon-polariton adiabatic propagation along the cone.

Both the processes so far described, the FIBM and the EBID ones, have been used to produce photonic crystal cavity and cone nano-waveguide on top of an atomic force microscopy (AFM) cantilever. Commercially available Si_3N_4 with 600 nm standard thickness cantilevers have been used and locally thinned in the area of the photonic crystal. The thinning process has been achieved by means of

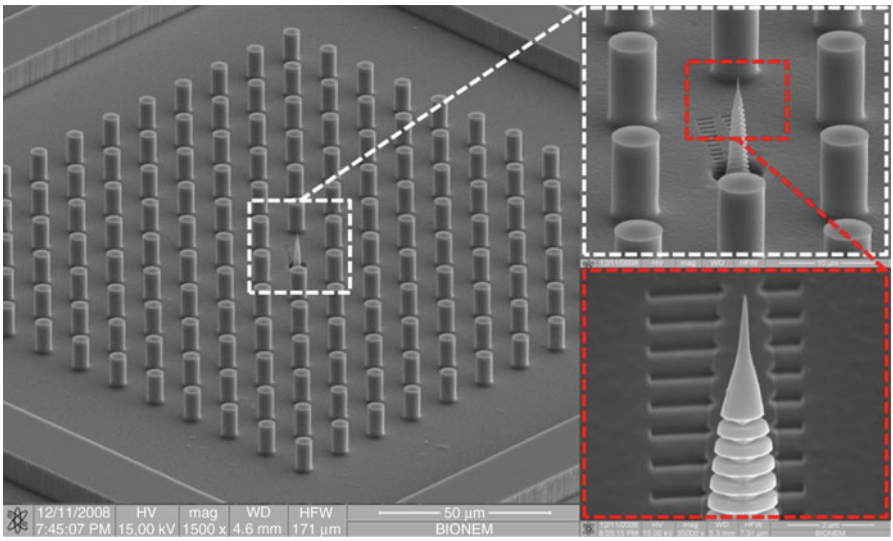

Fig. 19.24 Superhydrophobic chip with embedded a plasmonic metal cone-shaped nano-waveguide. One of the pillars of the superhydrophobic chip has been cone-reshaped by means of focus ion beam milling, and a coupling grating has been produced on one side of the cone using the same technique. Subsequently, a high-resolution plasmonic nano-waveguide has been fabricated on top of the reshaped pillar using electron beam-induced deposition (Picture kindly rearranged from Ref [93])

ion beam bombardment with large ions flux, and the area of the PC has been thinned down to 100 nm. Then, the PC has been realized by means of ion beam localized removal of material, thus opening air holes in the Si_3N_4 thinner area. Subsequently, the Pt–C cone has been fabricated in the middle of the PC optical cavity by means of EBID. A thin Ag layer (30 nm thickness) has been deposited over the sample and in particular over the cone, thus having a noble metal layer for the surface plasmon–polaritons propagation. Finally, the Ag layer has been removed only from the area of the photonic crystal, and not from the cone, with a gentle (small ion flux) ion beam bombardment of the PC surface. All these processes have been carried out using one only equipment, a FEI Nova Nanolab 600 dual beam system. This machine is, briefly speaking, constituted by two columns, an electron one along the vertical direction and a Ga^+ ions one that is tilted respect to the electrons one. The sample is mounted on a stage that can be tilted in the space, in order to have the sample perpendicular to the electron column or to the ion one, according to the column used for manufacturing the sample. The system is moreover equipped with a gas injection system that allows in the present case EBID in combination with the electron beam.

Similar plasmonic nano-waveguides have been also implemented in micropatterned superhydrophobic substrates. Micropatterned superhydrophobic substrates are made of regular arrays of pillars with typical dimensions in the 10 µm scale. As an example, the superhydrophobic pattern in Fig. 19.24 is

constituted by a triangular lattice of Si pillars with 5 μm diameter, 15 μm of lattice constant, and 50 μm of height.

Geometrical parameters can be adjusted in order to achieve higher contact angle once a drop of solution is deposited on the superhydrophobic surface. The superhydrophobic pattern is accomplished with standard, planar 2D lithographic techniques, made of optical lithography in combination with deep reactive ion etching process (Bosch process) [116]. Once produced, the superhydrophobic pattern has been processed using focus ion beam milling and electron beam-induced deposition. First of all the Si pillar in the middle of the pattern, which initially has a cylindrical shape, has been reshaped as a cone by means of FIBM: ion bombardment has been used to remove Si material from the cylindrical pillar until a cone is obtained. Subsequently, FIBM has been used to produce a far-field light coupling grating on one side of this large cone. The grating is necessary in order to couple the laser light coming from far-field with the plasmonic nano-waveguide (see further). At this point a plasmonic nanocone has been fabricated on top of the large cone by using EBID, as described above. It is worthy to say that the cone shaped from the cylindrical pillar by means of FIBM exhibits a regular cone shape, but the resolution achievable with this technique for the apex is much worse than the resolution of a cone produced by means of EBID. Finally, a thin Ag layer (20 nm) has been deposited on the whole sample area and obviously on the cone nano-waveguide, thus ensuring the presence of a noble metal layer for surface plasmon-polariton propagation.

Characterization of the Plasmonic Devices

As mentioned above, plasmonic cone-shaped nano-waveguides have attracted interest due to their ability to propagate and concentrate light beyond the diffraction limit. This fascinating effect is also accompanied by an increase of the propagating electromagnetic field as it approaches the apex tip, and smaller is the radius of curvature larger is the enhancing factor. Both these effects in turn produce significant advantages in optical-based techniques, such as Raman spectroscopy. In fact, by means of a proper use and configuration of the plasmonic nanocones, largely enhanced Raman signals can be recorded from very narrow areas, i.e., with spatial resolution higher than the spatial resolution imposed by the diffraction limit.

When laser light coming from the far-field is focused through an optical objective, the maximum spatial resolution achievable is of the order of half wavelength, and for visible light, we are in the 200–300 nm range. Instead, if light is properly coupled with the base of the plasmonic cone, surface plasmon polaritons are excited at the cone base and start to propagate along the cone towards the tip. Surface plasmon polaritons are oscillations of the electron gas within the metallic layer, which covers the nanocones (the 20 nm thick Ag layer), and these charge oscillations inside the metal layer are accompanied by an oscillating electromagnetic field just outside the metal surface. As predicted in Ref. [109], the surface plasmon-polariton experience, in the propagation along the cone, larger effective refractive index as they approach the apex. This in turn produces a slowing of their group velocity and consequently a plasmon accumulation occurs at the apex, with a high

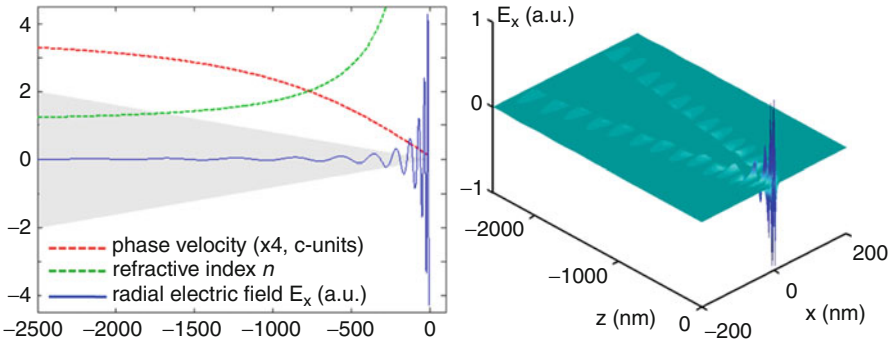

Fig. 19.25 Propagation of surface plasmon polaritons along the cone surface and plasmon accumulation at the tip of the cone. On the *left*, the behavior of both the effective refractive index and the phase velocity of the polaritons as a function of the position along the cone axis. The phase velocity goes to zero as the tip is approached. Also, the electric field in radial direction, termed E_x, calculated just outside of the cone, is reported as a function of the position along the cone axis: it is evident the strong enhancement achieved at the tip due to plasmon accumulation. On the *right*, a two-dimensional plot of the radial electric field: the field inside the cone is nearly zero and we have, just outside the cone, the electric field accompanying the plasmon polaritons. The enhancement is strongly localized around the tip of the cone, and the field soon decays as we move far from the tip (Picture kindly rearranged from Ref [3])

enhancement of the electric field which propagates along with the plasmon polaritons (Fig. 19.25).

The result is that the far-field light coupled to the base of the cone is concentrated in a narrow area comparable with the tip dimension, which is in the 2.5–5 nm range in the case of the cone shown in Fig. 19.20 and Fig. 19.23, much beyond the diffraction limit. Once at the tip, this electromagnetic field propagating with the surface polaritons decays again in free photons, due to the apex singularity. The resulting electromagnetic field can then produce Raman scattering from species very close to the tip, a Raman signal coming from a very narrow area which is of the same order of the tip size. As a result, it is possible to record Raman enhanced signals with a high spatial resolution, well beyond the diffraction limit.

This effect is strongly dependent on the geometry of the cone. First of all the cone has to produce an adiabatic compression of surface polaritons, thus meaning that the slope of the cone, i.e., the apex angle, has to be small enough to ensure a slowly varying effective refractive index. The other crucial point is the apex radius of curvature, which strongly affects the field enhancement. If we consider as field enhancement the ratio $|E_T|/|E_B|$, where E_T and E_B are respectively the electric field amplitudes at the tip and at the base of the cone, we obtain large enhancing factors only for tip radius below 5 nm (Fig. 19.26). Both these requirements are met by the cone fabricated on top of AFM cantilever (Figs. 19.20 and 19.23) and the cone embedded in the superhydrophobic surface (Fig. 19.24).

This working mechanism has been first demonstrated using the metal cone nano-waveguides fabricated on top of the AFM cantilever. Following the scheme

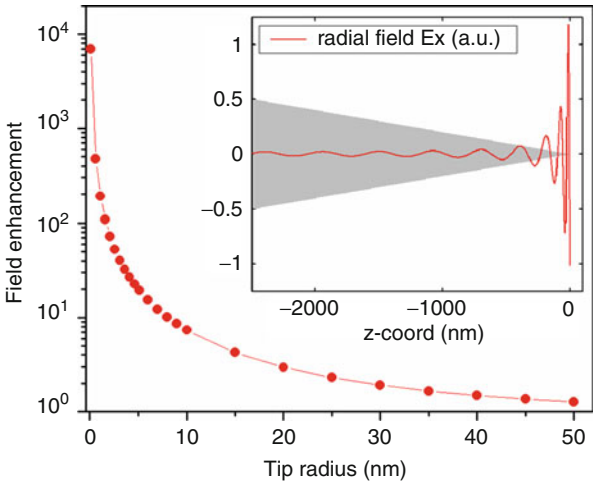

Fig. 19.26 Electric field enhancement at the cone tip as a function of the curvature radius of the tip itself. The calculations for the tip enhancement are based on the method proposed in Ref. [1]; the continuous line is just a guideline for eyes. As we can see from the graph, the curvature radius at the tip is a crucial parameter, and only for curvature radius below 10 nm significant enhancement factors are achieved. Keep in mind that Raman enhancement scales as the fourth power of the field enhancement factor (Picture kindly rearranged from Ref [3])

reported in Fig. 19.27, this device has been used to simultaneously record topographic and chemical data from a well-known sample [3]. The AFM cantilever has been mounted on an AFM machine and an infrared laser has been used to record the deflection of the AFM cantilever, thus recording the topography of the sample as usually done in AFM measurements. At the same time Raman measurements in transmission configuration are recorded. A laser light with wavelength $\lambda = 532$ nm has been focused on the photonic crystal cavity with a standard microscope condenser lens (numerical aperture NA = 0.35 and working distance of 70 mm), thus producing coupling between the far-field laser light and the base of the metal cone. Surface plasmon polaritons are excited at the base of the cone and propagate towards the tip, experiencing adiabatic slowing of the velocity and plasmon accumulation at the tip. This in turn produces a high enhancement of the electric field, which generates enhanced Raman signal from the sample that is close to the tip during the AFM measurement. Finally, the Raman signal is collected by a high numerical aperture objective placed at the bottom of the sample (immersion oil objective with NA = 1.4). This is made possible by the fact that the well-known sample is a transparent one and it consists of gratings of silicon nanocrystals having different pitches (from several micrometers to a sub-micrometer scale) obtained by laser melting of a silica substrate previously fabricated by plasma-enhanced chemical vapor deposition. The resulting sample is constituted by alternate stripes of SiO_x (taller) and Si (smaller) on a base of SiO_x substrate. The chemical mapping

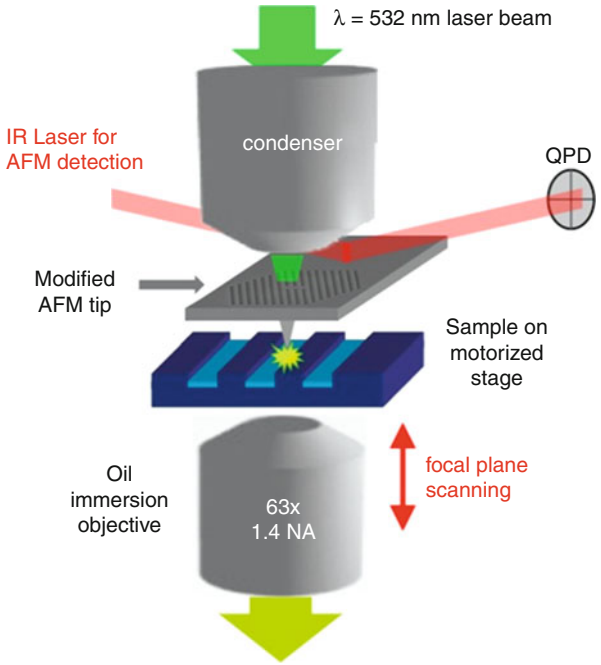

Fig. 19.27 Schematic picture of the experiment for simultaneous topographical and chemical mapping with high spatial resolution. An infrared laser is reflected by the *AFM* cantilever, and a quadrant photodiode (*QPD*) allows for measuring the cantilever deflection, thus measuring the topography of the sample as in *AFM* measurements. The tapping mode has been used for *AFM* recording. At the same time, a 532 nm wavelength laser is focused through a condenser lens on the photonic crystal cavity, thus exciting plasmon polaritons at the nanocone base. Polaritons propagate till the cone tip, where plasmon accumulation generates an intense and very narrow (below the diffraction limit) light spot. This light produces Raman scattering on the sample that is close to the tip, and the Raman signal is collected by a high numerical aperture objective, in transmission mode (Picture kindly reprinted from Ref. [3])

achieved by means of Raman spectroscopy depends on the fact that Si has a characteristic Raman peak at 520 cm^{-1} missing in SiO_x material.

To test the spatial resolution of this device for chemical mapping, the best fabricated tapered waveguide with an apex radius of curvature of 2.5 nm has been used. In this case, the expected theoretical field enhancement is ≈100 (Raman enhancement $\approx 1 \times 10^8$). The AFM–Raman setup has been operated in tapping mode and wet conditions (in distilled water) to measure simultaneously the topography and Raman intensity map by scanning the sample and acquiring Raman data across the lithographic structures, point by point. Figure 19.28 shows the results of simultaneous topographic and chemical mapping: it is clear from the topographical data that we are crossing the edge between a SiO_x stripe and a Si one, and at the same time, the collected Raman spectra show the transition between the distinctive Si spectra and the SiO_x ones (collected spectral region between 400 and

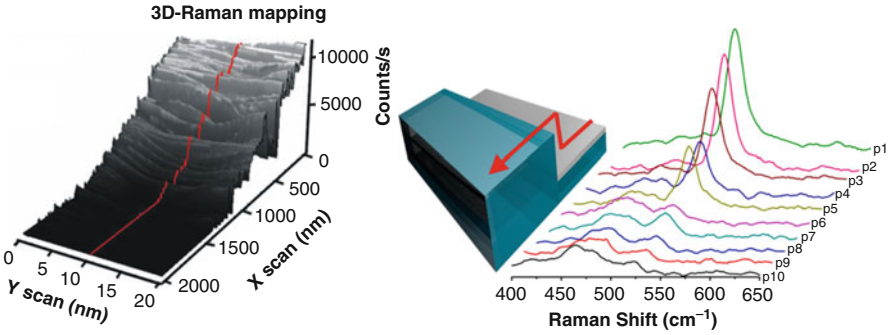

Fig. 19.28 Simultaneous topographic (*AFM*) and chemical (Raman spectroscopy) mapping of a test sample constituted by alternating stripes of SiO_x and Si with different height. On the *left* is the result of the topographic mapping, and on the *right* is the result of the chemical mapping. In the chemical mapping, the transition from Si, with a sharp Raman peak at 520 cm^{-1}, to SiO_x which exhibits a broader band at 480 cm^{-1} (and no Si peak) is clear. The scanning stepsize was 220 nm along the direction perpendicular to the stripes (Picture kindly reprinted from Ref. [3])

650 cm^{-1}). In Fig. 19.28, the AFM scan stepsize is 220 nm. A much higher spatial resolution acquisition is reported in Fig. 19.29, where the Si/SiO_x stripes have a much smaller pitch (at the sub-micrometer scale). In this case we center the Raman spectra at 520 cm^{-1} (collected spectral region between 500 and 540 cm^{-1}), and the presence of the peak at 520 cm^{-1} is an evidence of Si material. As we can see from the figure, as the topographical height of the sample decreases, the 520 cm^{-1} peak intensity increases, as expected when passing from SiO_x (taller) to Si (smaller) stripe. In this case the AFM scan stepsize is 7 nm, thus meaning that chemical mapping by means of an optical technique, Raman spectroscopy, has been achieved with a spatial resolution much beyond the diffraction limit of light.

As aforementioned, a similar device has been embedded also in a superhydrophobic pattern (Fig. 19.24) [93]. In this case the final goal is not the mapping of a surface, but the Raman-enhanced signal in a well-defined position. In this kind of device, a solution drop with a largely diluted solute is deposited on the superhydrophobic pattern. Due to the large contact angle, the drop of solution will stay only on the top of the pillars without wetting the bottom surface. As evaporation of the drop goes on, the diluted solute will be concentrated and finally released only on the top of few pillars. In the present case, where a sharp cone is present in the position of one of the pillar, the drop will concentrate the solute mainly on top of the cone apex, as thoroughly discussed in the supplementary material of Ref. [93]. Once the solution has been concentrated on top of this Raman enhancing antenna, it will be possible to detect very small starting concentrations, bringing molecules, which in the starting solution were not possible to probe, to a detectable level.

We have tested this device with a 1 fM lysozyme solution. More in details, a 160 nl droplet has been deposited on the superhydrophobic pattern

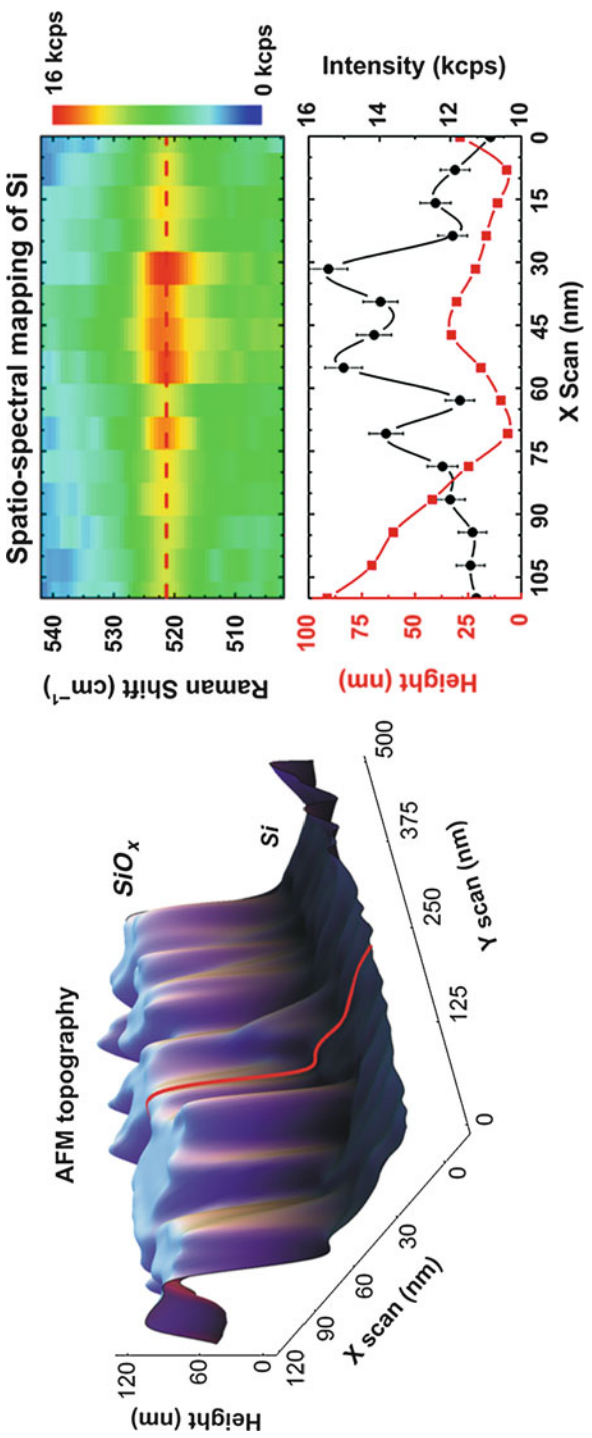

Fig. 19.29 Simultaneous topographic (*AFM*) and chemical (Raman spectroscopy) mapping of a test sample constituted by alternating stripes of SiO_x and Si with different height. On the *left* is the result of the topographic mapping. On the *right* is a color intensity map (*top*) of the 520 cm^{-1} Raman peak, typical of Si, as a function of the position; in the *bottom*, a graph showed the peak intensity together with the height profile data, showing that the Si peak is present where the sample height is smaller (corresponding to the Si stripe). The scanning stepsize was 7 nm along the direction perpendicular to the stripes, much beyond the diffraction limit of light (Picture kindly reprinted from Ref. [3])

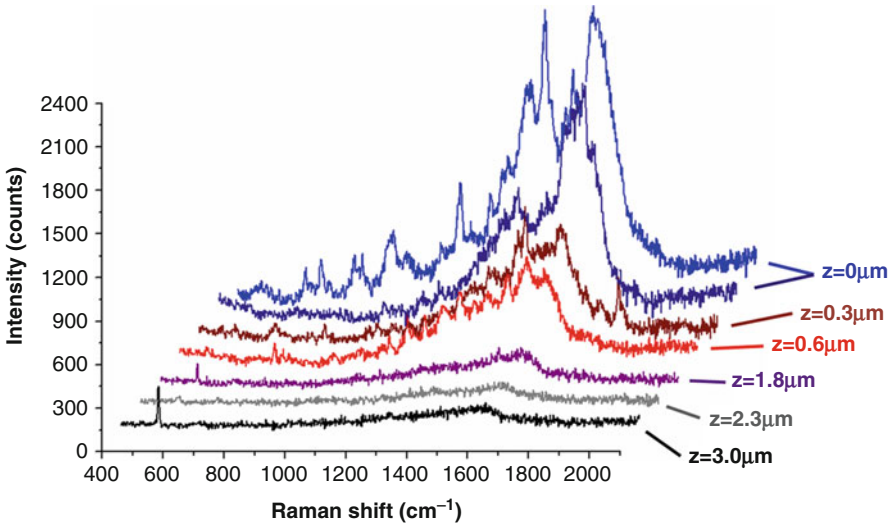

Fig. 19.30 Raman spectra recorded on 1 fM solution of lysozyme evaporated on top of a plasmonic cone-shaped nano-waveguide. The evaporation process took advantage of the presence of a micropatterned superhydrophobic surface. When the illumination and detection condition are the optimum, termed $z = 0$ μm, we have enhanced Raman signal with intense bands; as soon as we move far from the optimal conditions, the Raman bands soon decrease, and they are completely lost for z = 3.0 μm

by means of a microinjector coupled to a micromanipulator for aligning to the center of the pattern. At the end of the evaporation process that lasts few seconds due to the small amount of liquid, lysozyme accumulates on the silver cone. Only molecules very close to the tip are probed by Raman scattering, as the electric field enhancement soon decreases when moving from the tip apex. Far-field laser light at $\lambda = 532$ nm is coupled with the diffraction grating fabricated on one side of the largest Si cone (see Fig. 19.25). This excites surface plasmon polaritons in the thin silver layer, and they propagate till the cone apex. As before the cone is properly shaped in order to produce an adiabatic compression of polaritons with an enhanced electric field at the apex. For a tip with a curvature radius of 10 nm the expected amplification factor is ~35, which leads to a Raman enhancement of 1.5×10^6. The few lysozyme molecules deposited on the tip are probed by means of this enhanced Raman scattering, as a function of the focused laser along the z direction (which is the one of the optical axis). The recorded Raman spectra exhibit intense Raman bands when the coupling with the grating and the detection conditions are optimized, named $z = 0$ μm (see Fig. 19.30). When moving far from the polaritons excitation, i.e., from the coupling with the grating, the Raman bands soon decrease, and in a 3 μm range from the optimal condition of illumination, the Raman signal is completely lost.

Large Area Ordered and Reproducible SERS Substrate Based on Anodic Porous Alumina Template

Surface-enhanced Raman spectroscopy (SERS), an analytical technique, gained a lot of attraction in recent years due to its application in a wide range of fields. However, some drawbacks, such as lack of SERS enhancement for large areas and existence of random distribution of the hot spots, made SERS substrates not employed very often. A few works, reported in the past, overcame the hindering concerns by producing plasmonic devices following different techniques such as nanosphere lithography [117] and hole-mask lithography [118]. Herein, a new technique based on a gold-coated anodic porous alumina (gold APA) template is proposed to fabricate a convenient large-area SERS substrate. The porosity, wall thickness, and pore size of the APA template can be modulated by different fabrication parameters such as the electrolyte solution and etching time [119].

APA substrates with periodic hexagonal structures were fabricated by following different protocols, which allowed us to obtain different pore diameters and pore wall thickness. The fabricated APA substrates were used as a template for the preparation of nano-patterned gold surface, obtained by gold film deposition of 25 nm thickness, covering the APA features. The novelty of this work relies on the fabrication of reproducible large-area SERS substrates with wall thickness and pore-size down to 15 and 36 nm, respectively [64, 120]. The surface morphology of the SERS device was investigated by means of scanning electron microscopy (SEM) whereas the functioning as a SERS substrate was examined for different fluorescent molecules (cresyl violet (CV) and rhodamine6G (Rd6G)) after depositing them by chemisorption technique. The gold APA substrates were demonstrated to be an effective universal SERS substrate for analytical purpose.

APA substrates were prepared at +7 °C bath temperature with electrolyte stirring with aluminum sheet (250 μm) as the anode and platinum as the cathode, in the same electrochemical cell configuration as explained [121] (see Fig. 19.31). Firstly, the Al foil was electro-polished in a 1:5 v/v aqueous solution of $HClO_4$:C_2H_5O-H. A fast anodization process (1 h) was carried out in aqueous solutions of different acids (phosphoric, oxalic, and sulfuric acid) in order to achieve different pore diameter/wall thickness. A periodic structure can be observed on aluminum surface after removing the anodic oxide layer using the solution of phosphoric acid and chromic acid. Further, slow anodization during overnight was performed to attain a homogeneously formed pore structures on the aluminum foil.

In this work, the substrates were categorized in three parts: (a) large pore-size APA substrate utilizing H_3PO_4 acid (APA_Ph) at 130 V, (b) medium-sized pore APA using $H_2C_2O_2$ (APA_Ox) at 40 V, and (c) small-sized pore APA using H_2SO_4 (APA_Sul) at 25 V.

In order to make APA substrate as plasmonic devices, gold with 25 nm thickness was thermally evaporated from a tungsten boat onto these substrates (APA_Ph, APA_Ox, and APA_Sul). The substance of interest was deposited over resulting gold-coated APA substrates (termed 'Au-APA_Ph,' 'Au-APA_Ox,' and 'Au-APA_Sul,' respectively) using a chemisorption technique. In this process,

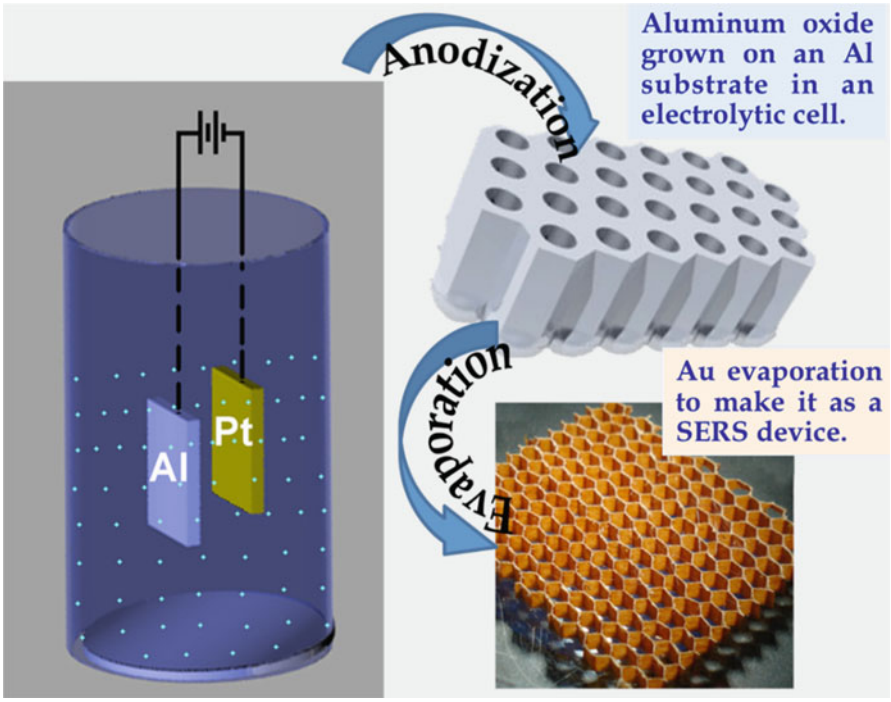

Fig. 19.31 Fabrication procedure of Au-APA substrate

the substrate was dipped into a solution containing the molecule of interest. After incubation, each substrate was removed from the solution and gently rinsed to remove excess molecules not attached directly to the metal surface. Thereafter, the samples were dried in N_2 flow and finally stored in a desiccator before SERS measurements. CV and Rd6G (10^{-6} M), fluorescent dyes, were employed as probe molecules.

SEM measurements (JSM-7500FA, Jeol, Japan) were also performed on the APA substrates, keeping a 15 kV acceleration voltage for the primary electron beam and collecting the topographic signal from the secondary electrons. For imaging of the specimens before gold coating the SEM was operated in low vacuum conditions (70–120 Pa residual chamber pressure) in order to prevent major static charging effects due to the impinging electron beam. A cartoon of honeycomb structure and SEM images of APA substrates before and after gold deposition are shown in Fig. 19.32.

SERS measurements were carried out by means of an inVia (Renishaw, New Mills, UK) microspectrometer, with a spectral resolution of 1.10 cm^{-1} with the help of a holographic grating of 1,800 grooves/mm. The samples were excited using the 633 nm laser wavelength (laser power 5.5–55 mW) in backscattering configuration through a 100× objective (NA-0.90) and with an accumulation time of 20 s. Spectral data were analyzed using Renishaw WiRE software 3.0.

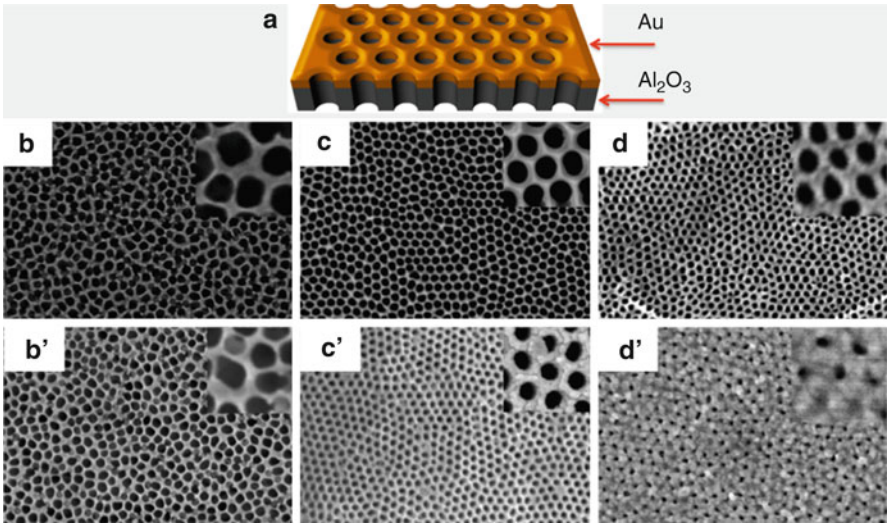

Fig. 19.32 (**a**) Cartoon image of Au-APA substrate. All the substrates before (**b**–**d**) and after (**b**'–**d**') gold deposition are shown

SEM images of all the Au-APA samples before and after gold deposition are shown in Fig. 19.32b–d and Fig. 19.32b'–d', respectively. CV and Rd6G, fluorescent dye molecules, were deposited using chemisorption technique to investigate the SERS activity of Au-APA substrates. The optical absorption spectra of both the molecules are shown in Fig. 19.32a.

Firstly, Raman spectrum of the bare substrate before depositing any molecule was performed and found a Raman spectrum within the noise level without any Raman peak (shown in inset of Fig. 19.33b), confirming the substrate free of any contamination. SERS spectra of CV molecules, deposited over different Au-APA substrates, are shown in Fig. 19.33b. In all the SERS spectra of the CV molecule, performed on Au-APA substrates with different pore diameters (15–160 nm) and wall thicknesses (36–100 nm) (Fig. 19.33b), the characteristic vibrational bands of CV are observed in the spectral range of 300–1,300 cm^{-1} [122]. Intense Raman bands centered at around 348, 591, 675, and 1,186 cm^{-1} can be attributed to the out-of-plane skeleton deformation, combination of in-plane N–H_2 and ring bending, ring deformation, and combination of N–H_2 rocking and C–H_x rocking, respectively [122, 123]. When the pore size/wall thickness of Au-APA substrate decreases from 160 nm/100 nm to 60 nm/40 nm, a significant increase in SERS intensity for the CV bands is observed with respect to the flat Au surface (inset of Fig. 19.33b). The band intensity, centered at 591 cm^{-1}, increases abruptly. It is shown in the inset of Fig. 19.33b the band intensity (591 cm^{-1}) variation for all the Au-APA substrates. It is found, finally, that when the pore size/wall thickness is around 100 nm/40 nm, the substrate behaves in its best conditions. SERS measurements were performed at different points of the large-area SERS device, showing

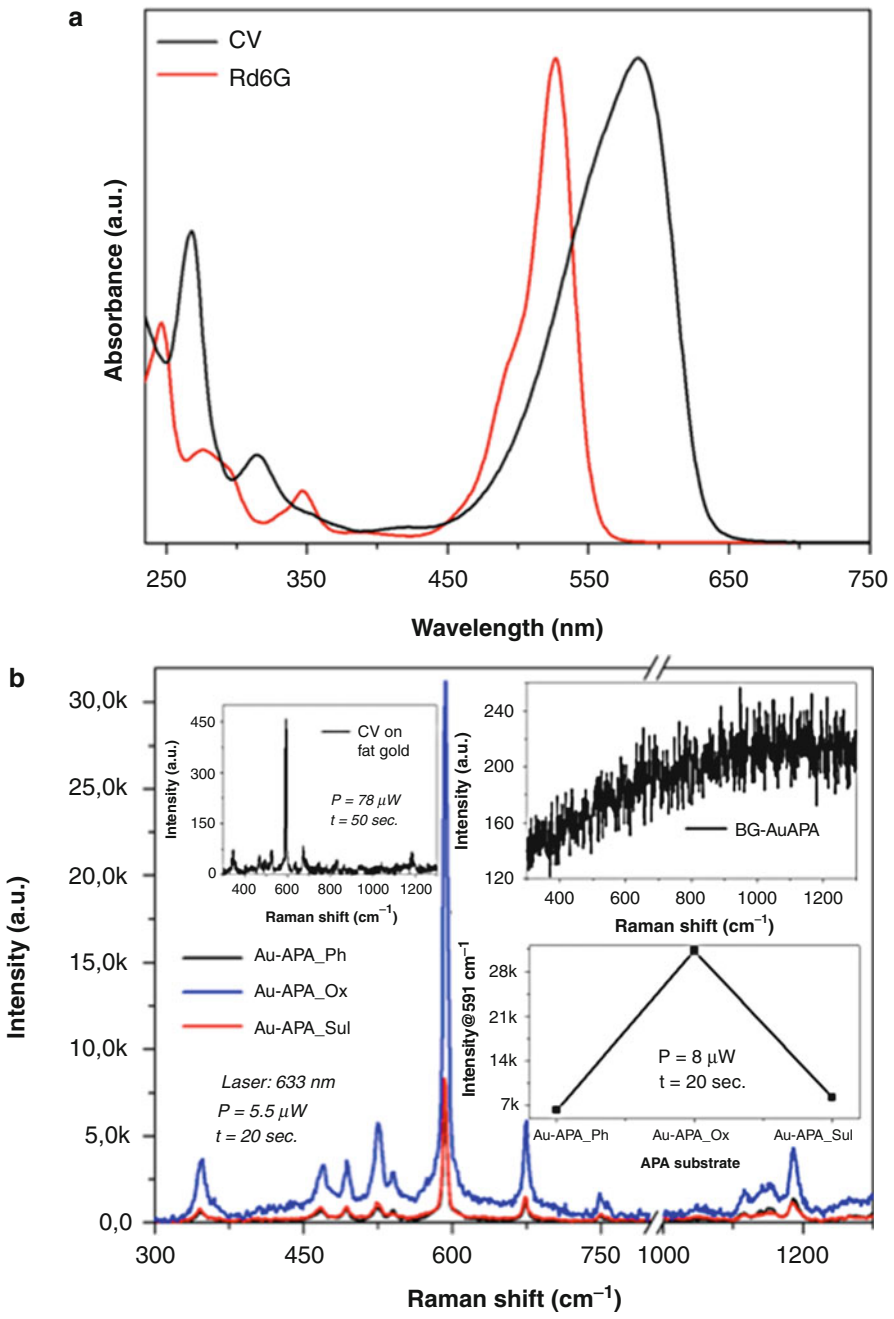

Fig. 19.33 (continued)

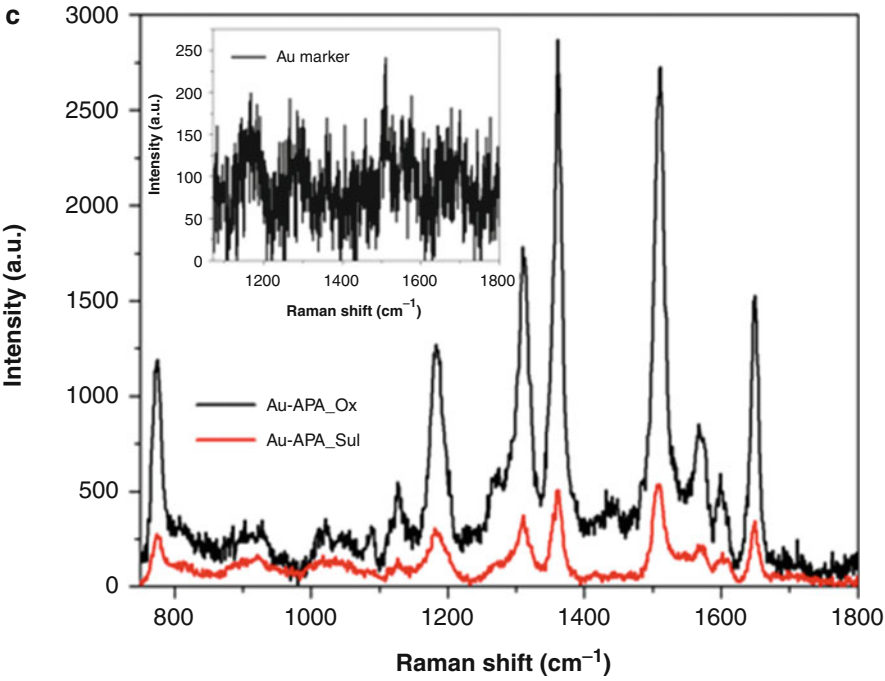

Fig. 19.33 (**a**) Optical absorption spectra for CV and Rd6G fluorescent molecules in the range of 230–750 nm. (**b**) SERS spectra of CV in the range of 300–1,300 cm^{-1}, deposited over all Au-APA substrates, in the inset bare SERS device Raman spectrum, reference measurement of CV on flat Au marker and the intensity variation of 591 cm^{-1} for all the Au-APA substrates are shown. (**c**) SERS spectra of Rd6G, deposited over Au-APA_Ox and Au-APA_Sul, are shown, in the inset, reference measurement of Rd6G deposited over Au marker is also shown

reproducible behavior of the device. This confirms the generation of hot spots in a controlled manner [64]. Considering this peak as a reference band to calculate the SERS enhancement factor, it is found to be around 10^4 with respect to the flat Au marker.

Furthermore, the substrates were investigated for Rd6G fluorescent dye molecule in order to demonstrate its efficiency for different molecules. Reference measurement for Rd6G molecule, deposited over flat Au marker, is shown in the inset of Fig. 19.33c. It shows few weak bands in the range of 1,000–1,800 cm^{-1}. SERS measurements were performed for the same, deposited over different Au-APA substrates (Fig. 19.33c). Figure 19.33 shows various characteristic peaks of Rd6G molecule within the spectral range [44, 124, 125]. In this case also, it is found that Au-APA_Ox is demonstrating its SERS enhancement much better than other Au-APA substrates.

To summarize, various home-built Au-APA substrates with varying pore size and wall thickness were utilized for large-area SERS substrates. CV and Rd6G fluorescent dye molecules were deposited using a chemisorption technique, through

which a monolayer of molecules can be achieved. It is observed that the AuAPA2 substrate (pore size = 59 ± 9, wall thickness = 40 ± 9) demonstrates the maximum SERS enhancement 'G'. The respective SERS enhancement factor 'G' is estimated to be 10^4 with respect to the flat Au marker. Additionally, the sensing efficacy of the fabricated SERS devices on different dyes and proteins (CV, Rd6G, and GFP in our case) opens the way for real application as a biosensor. Further research should be made in order to optimize 'G' on the basis of the substrate parameters of pore size, wall thickness, and thickness of the gold coating. The easy and inexpensive processing required for APA SERS fabrication would also make these substrates disposable, opening the way to their large-scale applications.

References

1. De Angelis F, Patrini M, Das G, Maksymov I, Galli M, Businaro L, Andreani LC, Di Fabrizio E (2008) A hybrid plasmonic-photonic nanodevice for label-free detection of a few molecules. Nano Lett 8:2321–2327
2. Zhang W, Cui X, Martin OJF (2009) Local field enhancement of an infinite conical metal tip illuminated by a focused beam. J Raman Spectrosc 40:1338–1342
3. De Angelis F, Das G, Candeloro P, Patrini M, Galli M, Bek A, Lazzarino M, Maksymov I, Liberale C, Andreani LC, Di Fabrizio E (2010) Nanoscale chemical mapping using three-dimensional adiabatic compression of surface plasmon polaritons. Nat Nanotechnol 5:67–72
4. Babadjanyan AJ, Margaryan NL, Nerkararyan Kh V (2000) Superfocusing of surface polaritons in the conical structure. J Appl Phys 87:3785–3788
5. Vaccaro L, Aeschimann L, Staufer U, Herzig HP, Dandliker R (2003) Propagation of the electromagnetic field in fully coated near-field optical probes. Appl Phys Lett 83:584–586
6. Ding W, Andrews SR, Maier SA (2007) Internal excitation and superfocusing of surface plasmon polaritons on a silver-coated optical fiber tip. Phys Rev A 75:063822
7. Neacsu CC, Bergewer S, Olmon RL, Saraf LV, Ropers C, Raschke MB (2010) Near-field localization in plasmonic superfocusing: a nanoemitter on a tip. Nano Lett 10:592–596; Gramotnev DK, Vogel MW, Stockman MI (2008) Optimized nonadiabatic nanofocusing of plasmons by tapered metal rods. J Appl Phys 104:034311
8. Lee JS, Han S, Shirdel J, Koo S, Sadiq D, Lienau C, Park N (2011) Superfocusing of electric or magnetic fields using conical metal tips: effect of mode symmetry on the plasmon excitation method. Opt Express 19:12342–12347
9. Proietti Zaccaria R, Alabastri A, De Angelis F, Das G, Liberale C, Toma A, Giugni A, Razzari L, Malerba M, Sun HB, Di Fabrizio E (2012) Fully analytical description of adiabatic compression in dissipative polaritonic structures. Phys Rev B 86:035410
10. Proietti Zaccaria R, De Angelis F, Toma A, Razzari L, Alabastri A, Das G, Liberale C, Di Fabrizio E (2012) Surface plasmon polariton compression through radially and linearly polarized source. Opt Lett 37:545–547
11. Corio P, Brown SDM, Marucci A, Pimenta MA, Kneipp K, Dresselhaus G, Dresselhaus MS (2000) Surface-enhanced resonant Raman spectroscopy of single-wall carbon nanotubes adsorbed on silver and gold surfaces. Phys Rev B 61:13202–13211
12. Davis TJ, Gomez DE, Vernon KC (2010) Evanescent coupling between a Raman-active molecule and surface plasmons in ensembles of metallic nanoparticles. Phys Rev B 82:205434
13. Fazio B, D'Andrea C, Bonaccorso F, Irrera A, Calogero G, Vasi C, Gucciardi PG, Allegrini M, Toma A, Chiappe D, Martella C, Buatier de Mongeot F (2011) Re-radiation

enhancement in polarized surface-enhanced resonant raman scattering of randomly oriented molecules on self-organized gold nanowires. ACS Nano 5:5945–5956
14. Chou SY, Ding W (2013) Ultrathin, high-efficiency, broad-band, omniacceptance, organic solar cells enhanced by plasmonic cavity with subwavelength hole array. Opt Express 21:A60–A76
15. Ojea-Jime'nez I, Lo'pez X, Arbiol J, Puntes V (2012) Citrate-coated gold nanoparticles as smart scavengers for mercury(II) removal from polluted waters. ACS Nano 6:2253–2260
16. Harris C, Kamat PV (2010) Photocatalytic events of CdSe quantum dots in confined media. Electrodic behavior of coupled platinum nanoparticles. ACS Nano 4:7321–7330
17. Persano A, De Giorgi M, Fiore A, Cingolani R, Manna L, Cola A, Krahne R (2010) Photoconduction properties in aligned assemblies of colloidal CdSe/CdS nanorods. ACS Nano 4:1646
18. Vasilantonakis N, Terzaki K, Sakellari I, Purlys V, Gray D, Soukoulis CM, Vamvakaki M, Kafesaki M, Farsar M (2012) Three-dimensional metallic photonic crystals with optical bandgaps. Adv Mater 24:1101
19. Christ A, Zentgraf T, Kuhl J, Tikhodeev SG, Gippius NA, Giessen H (2004) Optical properties of planar metallic photonic crystal structures: experiment and theory. Phys Rev B 70:125113
20. Neubrech F, Weber D, Katzmann J, Huck C, Toma A, Di Fabrizio E, Pucci A, Härtling T (2012) Infrared optical properties of nanoantenna dimers with photochemically narrowed gaps in the 5 nm regime. ACS Nano 6:7326
21. Razzari L, Toma A, Shalaby M, Clerici M, Proietti Zaccaria R, Liberale C, Marras S, Al-Naib IAI, Das G, De Angelis F, Peccianti M, Falqui A, Ozaki T, Morandotti R, Di Fabrizio E (2011) Extremely large extinction efficiency and field enhancement in terahertz resonant dipole nanoantennas. Opt Express 19:26088
22. Eigler D (1990) A new role for the STM. Science 250:1340–1341
23. Mock JJ, Barbic M, Smith DR, Schultz DA, Schultz S (2002) Shape effects in plasmon resonance of individual colloidal silver nanoparticles. J Chem Phy 116:6755–6759
24. Dasary SSR, Singh AK, Senapati D, Yu H, Ray PC (2009) Gold nanoparticle based label-free SERS probe for ultrasensitive and selective detection of trinitrotoluene. J Am Chem Soc 131:13806–13812
25. Alvarez-Puebla RA, Zubarev ER, Kotov NA, Liz-Marzan LM (2012) Self-assembled nanorod supercrystals for ultrasensitive SERS diagnostics. Nano Today 7:6–9
26. Sans V, Moskalenko A, Wilson K, Kozhevin V, Yavsin D, Kuzmin I, Gurevich S, Lapkin A (2011) SE(R)RS devices fabricated by a laser electrodispersion method. Analyst 136:3295–3302
27. Toma A, Chiappe D, Boragno C, Buatier de Mongeot F (2010) Self-organized ion-beam synthesis of nanowires with broadband plasmonic functionality. Phys Rev B 81:165436
28. Belardini A, Larciprete MC, Centini M, Fazio E, Sibilia C, Chiappe D, Martella C, Toma A, Giordano M, Buatier de Mongeot F (2011) Circular dichroism in the optical second-harmonic emission of curved gold metal nanowires. Phys Rev Lett 107:257401
29. Fazio B, D'Andrea C, Bonaccorso F, Irrera A, Calogero G, Vasi C, Gucciardi PG, Allegrini M, Toma A, Chiappe D, Martella C, Buatier de Mongeot F (2011) Re-radiation enhancement in polarized surface-enhanced resonant Raman scattering of randomly oriented molecules on self-organized gold nanowires. ACS Nano 5:5945
30. Chung AJ, Huh YS, Erickson D (2011) Large area flexible SERS active substrates using engineered nanostructures. Nanoscale 3:2903–2908
31. Kumar A, Hwang JH, Kumar S, Nam JM (2013) Tuning and assembling metal nanostructures with DNA. Chem Commun 49:2597–2609
32. Qiu T, Chu PK (2008) Self-selective electroless plating: an approach for fabrication of functional 1D nanomaterials. Mater Sci Eng R 61:59–77

33. Gao J, Tang F, Ren J (2005) Electroless nickel deposition on amino-functionalized silica spheres. Surf Coat Technol 200:2249–2252
34. Goia D, Matijevic E (1998) Preparation of monodispersed metal particles. New J Chem 22:1203–1215
35. Peng K, Zhu J (2004) Morphological selection of electroless metal deposits on silicon in aqueous fluoride solution. Electrochim Acta 49:2563–2568
36. Yang Y, Shi J, Kawamura G et al (2008) Preparation of Au-Ag, Ag-Au core-shell bimetallic nanoparticles for surface-enhanced Raman scattering. Scr Mater 58:862–865
37. Ye W, Chengmin S, Jifa T et al (2008) Self-assembled synthesis of SERS-active silver dendrites and photoluminescence properties of a thin porous silicon layer. Electrochem Commun 10:625–629
38. Palermo V, Jones D (2001) Morphological changes of the Si [100] surface after treatment with concentrated and diluted HF. Mater Sci Semicon Proc 4:437–441
39. Yae S, Nasu N, Matsumoto K et al (2007) Nucleation behavior in electroless displacement deposition of metals on silicon from hydrofluoric acid solutions. Electrochim Acta 53:35–41
40. Ye W, Chang Y, Ma C et al (2007) Electrochemical investigation of the surface energy: effect of the HF concentration on electroless silver deposition onto p-Si (111). Appl Surf Sci 253:3419–3424
41. Luk'yanchuk B, Zheludev NI, Maier SA et al (2010) The Fano resonance in plasmonic nanostructures and metamaterials. Nat Mater 9:707–715
42. Tao AR, Habas S, Yang P (2008) Shape control of colloidal metal nanocrystals. Small 4:310–325
43. Le Ru E, Etchegoin PG, Grand J et al (2008) Surface enhanced Raman spectroscopy on nanolithography-prepared substrates. Curr Appl Phys 8:467–470
44. Coluccio ML, Das G, Mecarini F et al (2009) Silver-based surface enhanced Raman scattering (SERS) substrate fabrication using nanolithography and site selective electroless deposition. Microelectron Eng 86:1085–1088
45. Das G, Mecarini F, Gentile F et al (2009) Nano-patterned SERS substrate: application for protein analysis vs. temperature. Biosens Bioelectron 24:1693–1699
46. Zhang X, Yonzon C, Duyne R (2006) Nanosphere lithography fabricated plasmonic materials and their applications. J Mater Res 21:1083–1092
47. De Angelis F et al (2011) Emerging fabrication techniques for 3D nano-structuring in plasmonics and single molecule studies. Nanoscale 3:2689–2696
48. Ashkin A (1970) Acceleration and trapping of particles by radiation pressure. Phys Rev Lett 24:156–158
49. Emiliani V (2005) Wave front engineering for microscopy of living cells. Opt Express 13(5):1395–1405
50. Cojoc D et al (2004) Multiple optical trapping by means of diffractive optical elements. Jpn J Appl Phys 43(6B):3910–3915
51. Garbin V et al (2007) Changes in microbubble dynamics near a boundary revealed by combined optical micromanipulation and high-speed imaging. Appl Phys Lett 90:114103
52. Cojoc D et al (2007) Properties of the force exerted by filopodia and lamellipodia and the involvement of cytoskeletal components. PLoS One 2(10):e1072
53. Sun HB, Kawata S (2004) Two-photon photopolymerization and 3D lithographic microfabrication, in advances in polymer science: NMR, 3-D analysis, photopolymerization, vol 170. Springer, Berlin, pp 169–273
54. Maruo S et al (2003) Force-controllable, optically driven micromachines fabricated by single-step two-photon microstereolithography. J Microelectromech Syst 12:533–539
55. Liberale C et al (2010) Micro-optics fabrication on top of optical fibers using two-photon lithography. IEEE Photonics Technol Lett 22:474–476
56. Takada K et al (2005) Improved spatial resolution and surface roughness in photopolymerization-based laser nanowriting. Appl Phys Lett 86:071122

57. Fuchs R (1975) Theory of the optical properties of ionic crystal cubes. Phys Rev B 11(4):1732–1740
58. Chirumamilla M et al (2012) Optimization and characterization of Au cuboid nanostructures as a SERS device for sensing applications. Microelectron Eng 97:189–192
59. Kreibig U, Vollmer M (1995) Optical properties of metal clusters, vol 25. Springer, Berlin
60. Kelly KL et al (2002) The optical properties of metal nanoparticles: the influence of size, shape, and dielectric environment. J Phys Chem B 107(3):668–677
61. Banaee MG, Crozier KB (2010) Mixed dimer double-resonance substrates for surface-enhanced Raman spectroscopy. ACS Nano 5(1):307–314
62. Chu Y, Banaee MG, Crozier KB (2010) Double-resonance plasmon substrates for surface-enhanced Raman scattering with enhancement at excitation and stokes frequencies. ACS Nano 4(5):2804–2810
63. Gopinath A et al (2009) Deterministic aperiodic arrays of metal nanoparticles for surface-enhanced Raman scattering (SERS). Opt Express 17(5):3741–3753
64. Das G et al (2012) Fabrication of large-area ordered and reproducible nanostructures for SERS biosensor application. Analyst 137(8):1785–1792
65. Rakic AD et al (1998) Optical properties of metallic films for vertical-cavity optoelectronic devices. Appl Opt 37(22):5271–5283
66. Johansson P, Xu H, Käll M (2005) Surface-enhanced Raman scattering and fluorescence near metal nanoparticles. Phys Rev B 72(3):035427
67. Witten T, Sander L (1981) Diffusion-limited aggregation, a kinetic critical phenomenon. Phys Rev Lett 47:1400–1403
68. Zhang Z, Lagally M (1997) Atomistic process in the early stages of thin-film growth. Science 276:377–383
69. Dawkins R, Ben-Avraham D (2001) Computer simulations of diffusion-limited reactions. Comput Sci Eng 3:72–76
70. Gentile F, Coluccio M, Toma A et al (2012) Electroless deposition dynamics of silver nanoparticles clusters: a diffusion limited aggregation (DLA) approach. Microelectron Eng 98:359–362
71. Witten T, Sander L (1983) Diffusion-limited aggregation. Phys Rev B 27:5686–5697
72. Hill SC, Alexander JID (1997) Modified diffusion-limited aggregation simulation of electrodeposition in two dimensions. Phys Rev E 56:4317–4327
73. Wu H, Lattuada M, Sandkuhler P et al (2003) Role of sedimentation and buoyancy on the kinetics of diffusion limited colloidal aggregation. Langmuir 19:10710–10718
74. Persson M, Yasuda H, Albergel J et al (2001) Modeling plot scale dye penetration by a diffusion limited aggregation (DLA) model. J Hydrol 250:98–105
75. Howells AR, Hung L, Chottiner GS et al (2002) Annealing of defects in crystals. Solid State Ion 150:53–62
76. Qiu T, Wu X, Siu G et al (2005) Self-assembled growth and green emission of gold nano whiskers. Appl Phys Lett 87:223115
77. Kuhn A, Argoul F (1995) Diffusion-limited kinetics in thin-gap electroless deposition. J Electroanal Chem 397:93–104
78. Qiu T, Wu X, Mei Y et al (2005) Self-organized synthesis of silver dendritic nanostructures via an electroless metal deposition method. Appl Phys A 81:669–671
79. Liu F-M, Green M (2004) Efficient SERS substrates made by electroless silver deposition into patterned silicon structures. J Mater Chem 14:1526–1532
80. Saltzmann M (2001) In drug delivery, vol pp. Oxford University Press, Oxford
81. Decuzzi P, Gentile F, Granaldi A et al (2007) Flow chamber analysis of size effects in the adhesion of spherical particles. Int J Nanomedicine 2:689–696
82. Haynes WM (1998) CRC handbook of chemistry and physics. CRC Press, Boulder
83. Gentile F, Battista E, Accardo A et al (2011) Fractal structure can explain the increased hydrophobicity of nanoporous silicon films. Microelectron Eng 88:2537–2540

84. Gentile F, Rocca RL, Marinaro G et al (2012) Differential cell adhesion on mesoporous silicon substrates. ACS Appl Mater 4:2903–2911
85. Meakin P (1984) Diffusion controlled deposition on surfaces: cluster size distribution, interface exponents, and other properties. Phys Rev B 30:4207–4214
86. Racz Z, Vicsek T (1983) Diffusion controlled deposition: cluster statistics and scaling. Phys Rev Lett 51:2382–2385
87. Gentile F, Moretti M, Limongi T et al (2012) Direct imaging of DNA fibers: the visage of double helix. Nano Lett 12:6453–6458
88. Han W, Byun M, Lin Z (2011) Assembling and positioning latex nanoparticles via controlled evaporative self-assembly. J Mater Chem 21:16968
89. Hejazi V, Nosonovsky M (2012) Wetting transitions in two-, three-, and four-phase systems. Langmuir 28:2173–2180
90. Cui Y (2001) Nanowire nanosensors for highly sensitive and selective detection of biological and chemical species. Science 293:1289–1292
91. Accardo A, Tirinato L, Altamura D, Sibillano T, Giannini C, Riekel C, Di Fabrizio E (2013) Superhydrophobic surfaces allow probing of exosome self organization using X-ray scattering. Nanoscale 5:2295–2299
92. Berry SM, Pabba S, Crest J et al (2011) Characterization and modeling of direct-write fabrication of microscale polymer fibers. Polymer 52:1654–1661
93. De Angelis F, Gentile F, Mecarini F et al (2011) Breaking the diffusion limit with superhydrophobic delivery of molecules to plasmonic nanofocusing SERS structures. Nat Photonics 5:682–687
94. Su B, Wang S, Wu Y et al (2012) Small molecular nanowire arrays assisted by superhydrophobic pillar-structured surfaces with high adhesion. Adv Mater 24:2780–2785
95. Accardo A, Gentile F, Mecarini F et al (2010) In situ X-ray scattering studies of protein solution droplets drying on micro- and nanopatterned superhydrophobic PMMA surfaces. Langmuir 26:15057–15064
96. Tucker TJ (1961) Behavior of exploding gold wires. J Appl Phys 32:1894
97. Willander M, Nur O, Zhao QX et al (2009) Zinc oxide nanorod based photonic devices: recent progress in growth, light emitting diodes and lasers. Nanotechnology 20:332001
98. Xu S, Wang ZL (2011) One-dimensional ZnO nanostructures: solution growth and functional properties. Nano Res 4:1013–1098
99. Atanasova P, Thomas Weitz R, Gerstel P et al (2009) DNA-templated synthesis of ZnO thin layers and nanowires. Nanotechnology 20:365302
100. Demming A, Brongersma M, Kim D-S (2012) Plasmonics in optoelectronic devices. Nanotechnology 23:440201
101. Willets KA, Van Duyne RP (2007) Localized surface plasmon resonance spectroscopy and sensing. Annu Rev Phys Chem 58:267–297
102. Liu N, Tang ML, Hentschel M et al (2011) Nanoantenna-enhanced gas sensing in a single tailored nanofocus. Nat Mater 10:631–636
103. Toma A, Das G, Chirumamilla M et al (2012) Fabrication and characterization of a -nanoantenna-based Raman device for ultrasensitive spectroscopic applications. Microelectron Eng 98:424–427
104. De Angelis F, Proietti Zaccaria R, Francardi M et al (2011) Multi-scheme approach for efficient surface plasmon polariton generation in metallic conical tips on AFM-based cantilevers. Opt Express 19:22268–22279
105. Biagioni P, Huang JS, Hecht B (2012) Nanoantennas for visible and infrared radiation. Rep Prog Phys 75:024402
106. Huang J-S, Kern J, Geisler P et al (2010) Mode imaging and selection in strongly coupled nanoantennas. Nano Lett 10:2105–2110
107. Panaro S, Toma A, Proietti Zaccaria R et al (2013) Design and top-down fabrication of metallic L-shape gap nanoantennas supporting plasmon-polariton modes. Microelectron Eng. doi:10.1016/j.mee.2013.02.014

108. Chen K-P, Drachev VP, Borneman JD et al (2010) Drude relaxation rate in grained gold nanoantennas. Nano Lett 10:916–922
109. Stockman MI (2004) Nanofocusing of optical energy in tapered plasmonic waveguides. Phys Rev Lett 93(13):137404(1)–137404(4)
110. Tormen M, Romanato F, Altissimo M et al (2004) Three-dimensional micro- and nanostructuring by combination of nanoimprint and X-ray lithography. J Vac Sci Technol B 22(2):766–770
111. Romanato F, Businaro L, Vaccari L et al (2003) Fabrication of 3D metallic photonic crystals by X-ray lithography. Microelectron Eng 67:479–486
112. Krauss TF, DeLaRue RM, Brand S (1996) Two-dimensional photonic-bandgap structures operating at near-infrared wavelengths. Nature 383:699–702
113. Vlasov YA, Bo XZ, Sturm JC et al (2001) On-chip natural assembly of silicon photonic bandgap crystals. Nature 414:289–293
114. Noda S, Fujita M, Asano T (2007) Spontaneous-emission control by photonic crystals and nanocavities. Nat Photonics 1:449–458
115. Van Dorp WF, Van Someren B, Hagen CW et al (2005) Approaching the resolution limit of nanometer-scale electron beam-induced deposition. Nanoletters 5(7):1303–1307
116. Gentile F, Das G, Coluccio ML et al (2010) Ultra low concentrated molecular detection using super hydrophobic surface based biophotonic devices. Microelectron Eng 87:798–801
117. Anker JN et al (2008) Biosensing with plasmonic nanosensors. Nat Mater 7:442
118. Shegai T et al (2012) Directional scattering and hydrogen sensing by bimetallic Pd–Au nanoantennas. Nano Lett 12:2464–2469
119. Parkhutik VP, Shershulsky VI (1992) Theoretical modelling of porous oxide growth on aluminium. J Phys D Appl Phys 25:1258
120. Das G et al (2012) Surface enhanced Raman scattering substrate based on gold-coated anodic porous alumina template. Microelectron Eng 97:383
121. Salerno M, Patra N, Cingolani R (2009) Use of ionic liquid in fabrication, characterization, and processing of anodic porous alumina. Nanoscale Res Lett 4:865
122. Vogel E, Gbureck A, Kiefer W (2000) Vibrational spectroscopic studies on the dyes cresyl violet and coumarin. J Mol Struct 177:550–551
123. Kudelski A (2005) Raman studies of rhodamine 6G and crystal violet sub-monolayers on electrochemically roughened silver substrates: do dye molecules adsorb preferentially on highly SERS-active sites? Chem Phys Lett 414:271
124. Mondal B, Saha SK (2010) Fabrication of SERS substrate using nanoporous anodic alumina template decorated by silver nanoparticle. Chem Phys Lett 497:89
125. Jensen L, Schatz GC (2006) Resonance Raman scattering of rhodamine 6G as calculated using time-dependent density functional theory. J Phys Chem A 110:5973